REPORT
doi:10.26443/seismica.v5i2.1556

SEISMICA

Performance of the 2021-2022 UPFLOW large ocean bottom seismometer array in the Azores-Madeira-Canary Islands region, Atlantic Ocean

Maria Tsekhmistrenko * [1], **Ana M.G. Ferreira** [1], **Miguel Miranda** [2,3], **Samaneh Baranbooei** [4], **Roberto Cabieces** [5], **Mafalda Carapuço** [2,3], **Carlos Corela** [6], **José Luis Duarte** [6], **Henrique Ferreira** [2], **Wolfram H. Geissler** [7], **Katrina Harris** [1], **Stephen P. Hicks** [1], **Kasra Hosseini** [1], **Kuan-Yu Ke** [8,9], **Frank Krüger** [10], **Dietrich Lange** [11], **Afonso Loureiro** [6,12], **Peter Makus** [8,9], **Augustin Marignier** [1], **Marta Neres** [2,6], **Luis Ramos** [2], **Theresa Rein** [10], **Alex Saoulis** [1], **David Schlaphorst** [6], **Mechita C. Schmidt-Aursch** [7], **Frederik Tilmann** [8,9]

[1]Department of Earth Sciences, University College London, London, UK, [2]Instituto Português do Mar e da Atmosfera (IPMA), 1749-077 Lisboa, Portugal, [3]Atlantic International Research Centre (AIR), Angra do Heroísmo, Portugal, [4]Dublin Institute for Advanced Studies (DIAS), School of Cosmic Physics, Dublin, Ireland, [5]Real Instituto y Observatorio de la Armada (ROA), San Fernando, Spain, [6]Instituto Dom Luiz (IDL), Faculdade de Ciências da Universidade de Lisboa, Portugal, [7]Alfred Wegener Institute, Helmholtz Centre for Polar and Marine Research, Bremerhaven, Germany, [8]Deutsches GeoForschungsZentrum GFZ, Potsdam, Germany, [9]Institute for Geological Sciences, Freie Universität Berlin, Germany, [10]University of Potsdam, Institute of Geosciences, Potsdam, Germany, [11]GEOMAR Helmholtz Centre for Ocean Research Kiel, Kiel, Germany, [12]Agência Regional para o Desenvolvimento da Investigação, Tecnologia e Inovação, Funchal, Portugal

Author contributions: *Conceptualization*: MT, AMGF. *Software*: MT, RC, KH, FT, FK, AMGF. *Data curation*: MT, RC, KH, FT, SPH, FK. *Investigation*: all authors. *Writing - original draft*: MT, AMGF. *Writing - Review & Editing*: all authors. *Visualisation*: MT, SPH, RC, CC, FT, AMGF. *Funding acquisition*: AMGF, MM.

Abstract The largest ocean bottom seismometer (OBS) experiment so far in the Atlantic Ocean occurred as part of the UPFLOW (Upward mantle flow from novel seismic observations) project to better constrain upward mantle flow, which is crucial to understanding global mantle dynamics. UPFLOW deployed 50 and recovered 49 OBSs in a $\sim$ 1,000 $\times$ 2,000 km^2 area in the Azores-Madeira-Canary islands region with a station spacing of $\sim$110-160 km between June 2021 and August 2022. Most instruments had three-component broadband seismic sensors and hydrophones, and three different designs of OBS frames were used. Our analysis shows $\sim$91 % data completeness. Vertical-component long-period noise (T>$\sim$30s) is reduced compared to previous experiments. The orientations of horizontal components were estimated from the polarisation of long-period body and surface waves from teleseismic events. Earth's free oscillations with frequencies as low as $\sim$1.8 mHz are observed following two $M_w > 8$ earthquakes, and the signal-to-noise ratio of these observations is enhanced after applying tilt and compliance corrections. We show illustrative recordings and spectrograms of teleseismic and local events as well as non-seismic signals (whales, instrument resonances), demonstrating the wide variety and richness of UPFLOW data and their potential to address many outstanding questions in solid Earth sciences, oceanography, and marine biology.

Non-technical summary Seismometers are instruments that record ground motion, and by analysing the data they capture, one can gain insights into the structures spanning from the Earth's core to its surface. In the past decades, seismology has experienced an explosion of dense land seismic networks. Yet, vast regions of our planet are still sparsely covered and therefore poorly understood: the oceans and the Earth's structure beneath them. Conducted in 2021-22, UPFLOW (Upward mantle flow from novel seismic observations) was the largest ocean bottom seismometer (OBS) deployment carried out so far in the Atlantic Ocean. Thanks to an international collaboration between institutions from five European countries (Germany, Ireland, Portugal, Spain, and the UK), UPFLOW deployed 50 ocean bottom seismometers (OBSs) in a $\sim$ 1,000 $\times$ 2,000 km^2 area in the Azores-Madeira-Canary Islands region in June 2021 and recovered 49 of them after $\sim$14 months. The ultimate goal of the experiment is to better understand upward mantle flow and the geodynamics of the region. In this study, we present the data acquired by the UPFLOW experiment, assess their quality and provide an overview of the recorded observations. We compare our data with those from other experiments and discuss their potential for upcoming studies.

Production Editor:
Yen Joe Tan
Handling Editor:
Suzan van der Lee
Copy & Layout Editor:
Hannah F. Mark

Received:
January 13, 2025
Accepted:
February 15, 2026
Published:
August 5, 2026

1 The UPFLOW project and experiment

1.1 Objectives and geophysical targets

The overarching goal of the UPFLOW project is to develop new high-resolution seismic imaging methods along with new ocean bottom seismometer (OBS) data collection (Ferreira et al., 2026). Further, the primary objectives of the UPFLOW OBS experiment are to investigate vertical mantle flow, its geometry, its interaction with the mid-ocean ridge and the lithosphere in the Azores-Madeira-Canary Islands region, and deep Earth structures, such as the African Large Low Seismic Velocity Province (LLSVP). Previously, these knowledge gaps

*Corresponding author: m.tsekhmistrenko@gmail.com

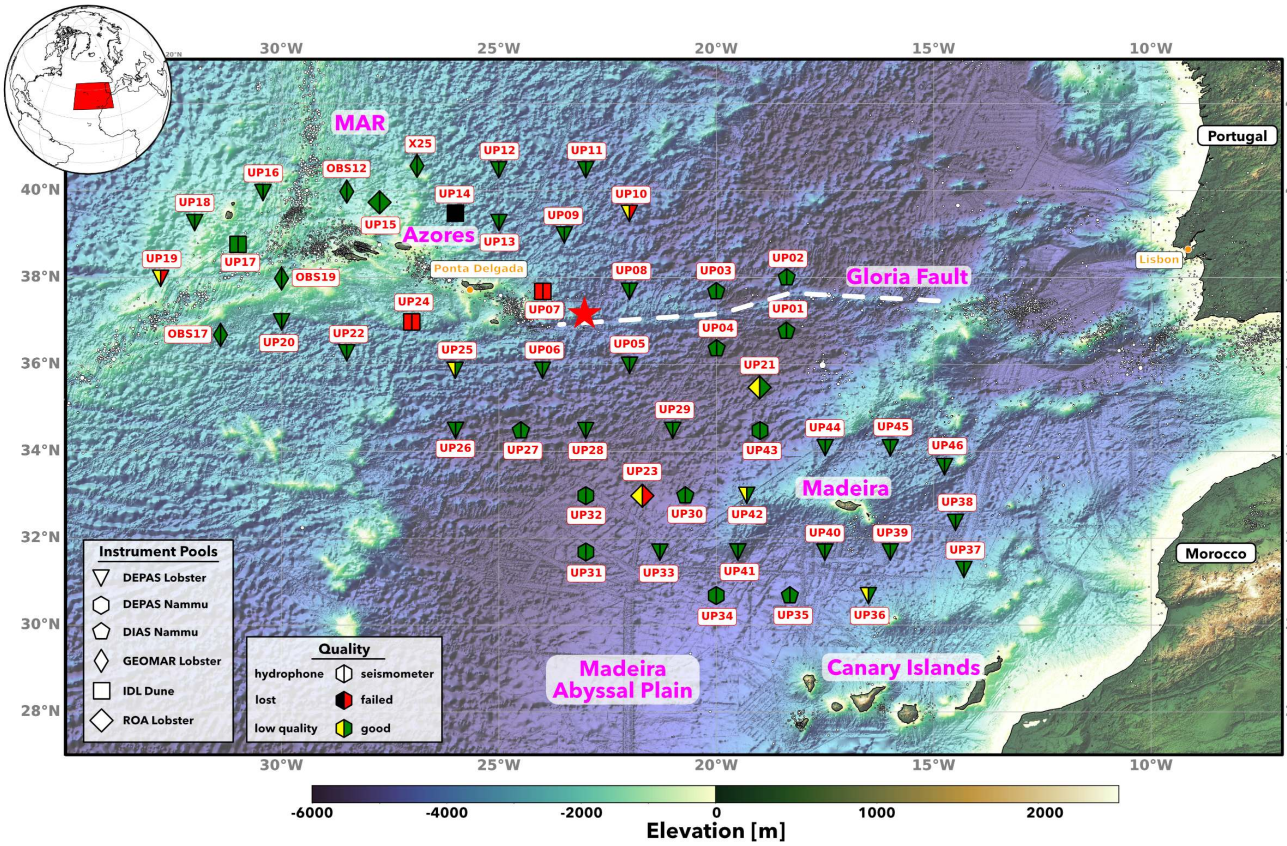

Figure 1 Map of the UPFLOW experiment. The different symbols show the location of UPFLOW's OBS stations, with different geometrical shapes representing different instrument pools, while the colour indicates the data quality, which is explained in Section 3. The left side of the symbol represents the data quality of the hydrophone component, while the right side represents the data quality of the three seismometer components. The map also displays seismicity data from 1970 to 2022 (white circles) obtained from the FDSN event catalogue (FDSN Web Services, n.d.) and downloaded with obspyDMT (Hosseini and Sigloch, 2017). Recent seismicity in 2022 is sourced from IPMA. The red star (close to UP07) shows the approximate location of an ML 1.7 local event in the Gloria Fault region. Fig. 8 shows the corresponding waveforms. MAR: Mid-Atlantic Ridge. The bathymetry was extracted from ETOPO (NOAA National Centers for Environmental Information, 2022).

have been challenging to investigate due to poor data coverage.

The Azores-Madeira-Canary Islands region, characterised by multiple potential mantle plumes, is still underexplored and poorly understood. While a deep mantle plume rising from the lower mantle beneath the Canary Islands seems to consistently appear in many seismic tomography models (Montelli et al., 2004; Marignier et al., 2020; Civiero et al., 2021), the situation is less clear beneath the Madeira and the Azores archipelagos. For Madeira, the proximity to the Canary Islands (∼300 km) and the limited resolution of existing tomography models have hindered efforts to probe the existence of deep plume structures in the area. Regarding the Azores, some tomography models suggest a lower mantle plume beneath the region, whereas others only show low velocity anomalies confined to the upper mantle (see, e.g., the study of Yang et al., 2006, which used multiple tomography models). Some studies have suggested the presence of a dying plume beneath the Azores (Silveira et al., 2006), while others attribute the region's magmatism exclusively to shallower convection and lithospheric processes, implying the absence of a deep mantle plume (Neves et al., 2013). The origin of a possible mantle plume beneath the Azores and the role of magmatic intrusions, small-scale convection, plume-lithosphere and plume-ridge interactions are topics of ongoing debate (e.g. Cannat et al., 1999; Gente et al., 2003; Beier et al., 2015; Genske et al., 2016). Beneath the Canary Islands, the lateral extent and vertical continuity of the plume-like anomaly in existing tomography models remain uncertain. Moreover, the relationship between the mantle upwelling beneath the Canary Islands and the nearby Madeira Island is also unclear. We aim to address these issues with the unique OBS data collected by the UPFLOW experiment.

1.2 OBS experiment

The UPFLOW experiment (Fig. 1) used the *R/V Mário Ruivo*, the Portuguese national scientific vessel operated by IPMA (Instituto Português do Mar e da Atmosfera) (The Portuguese Institute for Sea and Atmosphere, I. P. , 2023), covering a total distance of around 9,800 km in each deployment and recovery expedition. The experiment involved collaboration among institutions in five different countries: Portugal (IPMA; IDL, Instituto Dom Luiz; University of Lisbon; ISEL, Instituto Superior de Engenharia de Lisboa), Ireland (DIAS, Dublin Institute for Advanced Studies), UK (UCL, University Col-

Station	Pool & type	Deployed		Depth	Deployment	Recovery	Total days	Skew	Sampling rate	Preferred	Data
		Lat [°]	Lon [°]	GMRT [m]	Date	Date	recorded	[s]	Sm; Hyd [Hz]	Orientation [°]	completeness [%]
OBS12	GEOMAR	40.000	-28.500	2098	21.06.21	14.08.22	351	-7.59	100	3 ± 3	83.0
OBS17	GEOMAR	36.700	-31.401	2649	20.06.21	17.08.22	242	-7.12	100	188 ± 2	57.0
OBS19	GEOMAR	38.000	-30.000	1919	20.06.21	15.08.22	369	6.00	100	196 ± 5	87.0
UP01	DIAS	36.784	-18.384	5457	16.07.21	05.08.22	386	-2.74	250	44 ± 5	100.0
UP02	DIAS	38.017	-18.383	4841	17.07.21	06.08.22	386	1.39	250	148 ± 7	100.0
UP03	DIAS	37.700	-19.998	4549	17.07.21	06.08.22	386	6.75	250	159 ± 3	100.0
UP04	DIAS	36.386	-19.994	5272	17.07.21	07.08.22	387	7.22	250	71 ± 6	100.0
UP05	DEPAS	36.001	-21.997	4223	18.07.21	07.08.22	386	-12.64	100	173 ± 2	100.0
UP06	DEPAS	35.883	-24.001	4435	18.07.21	08.08.22	387	7.95	100	194 ± 4	100.0
UP07	IDL	37.701	-23.999	3215	19.07.21	08.08.22	224	0.34	250; 100	344 ± 1	58.0
UP08	DEPAS	37.700	-22,000	4335	19.07.21	09.08.22	387	-9.80	100	206 ± 3	100.0
UP09	DEPAS	38.999	-23.498	3874	20.07.21	09.08.22	386	-10.05	100	325 ± 4	100.0
UP10	DEPAS	39.501	-22.000	4407	20.07.21	10.08.22	387	-12.14	100	N/A	100.0
UP11	DEPAS	40.500	-23.000	4216	21.07.21	10.08.22	387	-8.57	100	277 ± 4	100.0
UP12	DEPAS	40.500	-25.000	3452	21.07.21	11.08.22	387	0.63	100	197 ± 5	100.0
UP13	DEPAS	39.285	-24.999	3303	21.07.21	12.08.22	389	-0.80	100	232 ± 3	100.0
UP14	IDL	39.500	-26.000	2986	22.07.21	N/A	N/A	N/A	250	N/A	0.0
UP15	ROA-UCM	39.750	-27.750	1966	22.07.21	13.08.22	327	N/A	50	180 ± 2	84.0
UP16	DEPAS	39.977	-30.430	1440	23.07.21	14.08.22	388	-15.48	250	29 ± 4	100.0
UP17	IDL	38.782	-31.000	1772	23.07.21	15.08.22	389	-4.66	250	170 ± 6	91.1
UP18	DEPAS	39.283	-31.999	1954	23.07.21	15.08.22	389	-13.24	100	304 ± 2	100.0
UP19	DEPAS	38.000	-32.782	1825	24.07.21	18.08.22	364	-0.53	100	N/A	50.1
UP20	DEPAS	36.999	-29.999	3316	24.07.21	18.08.22	391	-20.56	250	145 ± 5	100.0
UP21	ROA-UCM	35.499	-19.000	5319	07.08.21	01.09.22	391	0.52	50	116 ± 7	99.8
UP22	DEPAS	36.284	-28.501	3305	25.07.21	19.08.22	391	-0.32	100	127 ± 3	100.0
UP23	ROA-UCM	32.999	-21.700	5238	02.08.21	27.08.22	391	0.00	50	N/A	99.8
UP24	IDL	36.997	-27.002	2526	25.07.21	19.08.22	219	N/A	250; 100	163 ± 4	56.0
UP25	DEPAS	35.884	-26.000	4144	25.07.21	23.08.22	395	-7.60	100	278 ± 5	100.0
UP26	DEPAS	34.500	-26.000	5132	21.07.21	24.08.22	229	5.12	100	57 ± 3	57.0
UP27	DIAS	34.498	-24.501	4912	26.07.21	24.08.22	395	-17.99	250	136 ± 7	100.0
UP28	DEPAS	34.501	-23.001	4983	26.07.21	25.08.22	339	-8.46	100	275 ± 12	85.0
UP29	DEPAS	34.500	-21.000	5257	27.07.21	25.08.22	395	-11.28	100	180 ± 3	100.0
UP30	DIAS	32.999	-20.710	5028	02.08.21	27.08.22	391	N/A	250	238 ± 8	90.4
UP31	DEPAS N	31.700	-23.001	5185	02.08.21	26.08.22	390	-17.49	100	301 ± 2	100.0
UP32	DEPAS N	33.001	-22.999	5327	01.08.21	26.08.22	391	-13.96	100	128 ± 5	100.0
UP33	DEPAS	31.699	-21.300	4948	03.08.21	27.08.22	390	5.93	100	13 ± 2	100.0
UP34	DEPAS N	30.700	-20.000	4799	03.08.21	28.08.22	391	-5.81	100	46 ± 7	95.0
UP35	DIAS	30.701	-18.302	4600	04.08.21	28.08.22	390	-10.84	250	240 ± 5	100.0
UP36	DEPAS	30.699	-16.501	4236	04.08.21	29.08.22	391	-9.93	100	183 ± 3	100.0
UP37	DEPAS	31.299	-14.301	3652	05.08.21	29.08.22	390	-7.64	250	84 ± 6	100.0
UP38	DEPAS	32.383	-14.501	4389	05.08.21	30.08.22	391	-12.94	100	168 ± 3	100.0
UP39	DEPAS	31.700	-16.001	4435	05.08.21	30.08.22	391	-12.94	100	332 ± 4	100.0
UP40	DEPAS	31.700	-17.498	4513	06.08.21	30.08.22	390	-5.67	100	345 ± 3	100.0
UP41	DEPAS	31.700	-19.501	4375	06.08.21	31.08.22	391	-10.28	100	91 ± 6	100.0
UP42	DEPAS	33.001	-19.301	3855	06.08.21	31.08.22	391	-11.52	100	72 ± 6	100.0
UP43	DEPAS N	34.500	-19.000	5080	07.08.21	01.09.22	391	-21.71	100	81 ± 4	100.0
UP44	DEPAS	34.099	-17.499	4268	08.08.21	02.09.22	391	-18.74	100	319 ± 8	100.0
UP45	DEPAS	34.100	-16.000	4018	08.08.21	02.09.22	391	-15.26	250	115 ± 4	91.1
UP46	DEPAS	33.667	-14.749	3994	08.08.21	02.09.22	391	4.68	100	195 ± 5	100.0
X25	GEOMAR	40.591	-26.877	2519	21.06.21	13.08.22	320	4.53	100	173 ± 7	76.0

Table 1 Overview of the 50 UPFLOW OBS stations. Depths are based on the Global Multi-Resolution Topography (GMRT) at the station location (Ryan et al., 2009). All OBS clocks were synchronised to GPS time at deployment. The time difference between the GPS and OBS clocks at recovery is shown in the "skew" column. The seismometer (Sm) and hydrophone (Hyd) sampling rates are provided in Hz. Faulty stations are indicated in red. Data completeness represents the percentage of time recorded between the deployment and recovery dates, considering all four components. If this percentage is less than 100 %, it indicates the instrument stopped prematurely, or the recording was incomplete (gaps). For the entire UPFLOW experiment, the data completeness is 91.2 %, which also includes 0 % from UP14. Excluding the lost and faulty stations (stations marked in red), data completeness is 95.5 %. All DIAS stations have NAMMU OBSs, all GEOMAR stations have LOBSTERs, and the DEPAS pool has two different OBS designs (DEPAS: LOBSTER; DEPAS N: NAMMU). See Table 2 for details about instrumentation and frame design types. The column with "Preferred orientation" shows the horizontal component orientation estimates obtained in this study (Section 4.1).

lege London), Spain (ROA-UCM, Real Instituto y Observatorio de la Armada-Universidad Complutense de Madrid), and Germany (University of Potsdam; GFZ, Deutsches GeoForschungsZentrum; GEOMAR; AWI, Alfred Wegener Institute). Five different institutions provided the 50 free-fall OBSs used in the experiment (Table 1). In contrast to previous experiments targeting mantle plumes, where stations were closely clustered around a specific island of interest (e.g., PLUME Hawaii, Wolfe et al. 2009 and ISOLDE, Schlömer et al. 2017), UPFLOW had station spacings of approximately 110 km to 160 km, surrounding multiple islands (Fig. 1). This wider target area required a large array aperture, designed to image the seismic structure from the seafloor to the lower mantle. About one-third of the OBSs were deployed on the triangular-shaped Azores Plateau, including the Azores triple junction, at water depths down to around 2000 m. The remaining OBSs were deployed at water depths of 4000 m to 5000 m, mainly on the Madeira Abyssal Plain and along the Gloria Fault.

Following the recovery of the 49 OBSs, all stations and their data underwent thorough quality control and preliminary analysis to prepare the data for further scientific investigations, with a substantial part performed onboard the ship. Data were compared according to instrument type and also with results from previous OBS studies. This report documents the key findings from our data analysis and makes recommendations for future OBS data analyses.

2 Instrumentation

Most instruments were equipped with three-component broadband seismic sensors and hydrophones, while three different designs of OBS frames were utilised: LOBSTER, NAMMU, and DUNE (Fig. 2). The latter is a prototype OBS frame designed and built by IDL, and this experiment marks its first long-term deployment.

Apart from three OBSs from IDL and one from ROA-UCM, all UPFLOW stations were equipped with broadband Trillium Compact OBS seismometers manufactured by Nanometrics (see Table 2). They have a flat response from 0.0083 Hz (120 s) to 50 Hz; see Figures with example instrument response in the supplementary information (Fig. S1). The OBSs were equipped with HighTech HTI-04-PCA ULF hydrophone sensors, with a flat response in the frequency range from 0.01 Hz (100 s) to 8 kHz. The datalogger 6D6 from K.U.M. was used in all instruments except for the ROA-UCM and two of the DUNE OBSs. The ROA-UCM OBSs included legacy SEND Geolon MCS recorders. The prototype DUNE OBSs included permutations of different sensors and recorders. The Güralp Minimus (recorder) and Certis (sensor) were used in DUNE stations UP07 and UP24, and a 6D6 datalogger with Silicon Audio MEMS (micro-electromechanical systems) accelerometer was used in DUNE OBSs UP14 and UP17. This instrument integrates the mechanics of conventional geophones with MEMS sensors to create a seismic sensor developed originally for ocean-bottom applications.

70 % of UPFLOW stations comprised the LOBSTER (Long-term OBS for Tsunami and Earthquake Research) instruments manufactured by K.U.M. The LOBSTER model features cylindrical orange syntactic floating units held together by a titanium frame (Fig. 2, right). These floating units house various sensors, recording units and batteries within titanium tubes of different sizes (Schmidt-Aursch and Haberland, 2017). Hydrophones were attached to the recorder tube or the top of the frame. The seismometer is positioned between two floating units and anchored to the frame to enhance its coupling to the ocean floor. To facilitate recovery, an attached buoy is typically used and connected to the OBS via a rope. However, past experiments have revealed that free-floating buoys generate a detectable resonance (Stähler et al., 2018; Essing et al., 2021). For UPFLOW, a new deployment configuration was trialled where custom-made blue tarpaulin sheets secured the head buoys towards the frame to minimise rope resonance (see Fig. 2 right); the tarp unfolds when the OBS is released from the anchor, freeing the head buoy during recovery. This procedure was followed for all the LOBSTER OBSs except those from the GEOMAR pool (4 instruments), which were deployed on a separate cruise leg in June 2021.

The smaller NAMMU OBS model from K.U.M. (Fig. 2, left) employs similar principles as the LOBSTER (Schmidt-Aursch and Haberland, 2017). The seismometer and datalogger, however, are surrounded by syntactic foam buoyancy elements, offering some protection against external forcing such as ocean currents and avoiding potential damage resulting from contact with the ship's side.

The DUNE model (Fig. 2, middle) is a prototype from IDL. The instrument's specific circular diameter aims to minimise noise resonance caused by ocean waves and currents (Corela et al., 2023). Components are enclosed within the orange cylinder to minimise water vortices and subsequent drag and lift effects. Unlike the LOBSTER and NAMMU models, the orange cylinder of the DUNE instrument does not provide buoyancy for recovery. Instead, buoyancy is achieved by the glass spheres that house the batteries, datalogger, sensors and acoustic releaser. Upon reaching the surface, a snap-up flag, flasher, and radio beacon are activated. A pop-up flag that is triggered upon OBS release from the seafloor prevents the flag from generating noise due to seafloor currents, which can be substantial in the LOBSTER and NAMMU models (Stähler et al., 2016, 2018; Corela et al., 2023). A notable distinction between the DUNE model and the other OBS models used in the UPFLOW experiment is its release mechanism. In this case, instead of a retractable bolt, a burn wire mechanism is employed. A steel wire blocks the release mechanism. When voltage is applied to the release frame and the wire, a current path is established through the salt water, causing the galvanic corrosion of the wire until it finally breaks, releasing the instrument from its anchor. This release mechanism is similar to the one utilised in the French INSU (Stähler et al., 2016) and US (OBSIC) instruments.

3 Instrument performance

Fig. 1 shows the station information using colour coding to indicate performance: green for stations where all data were good and usable, yellow for stations that were noticeably noisier than others but still usable, red for stations where most or all data were unusable and black for stations that were lost or broken. This colour coding, similar to that used by Stähler et al. (2016), facilitates a quick performance assessment. The next section provides a detailed explanation of how we approached the station performance analysis.

Figure 2 Comparison of OBS types used in the UPFLOW experiment. From left to right: NAMMU (provided by DEPAS and DIAS), DUNE (prototype provided by IDL), and LOBSTER (provided by DEPAS, GEOMAR, and ROA-UCM). Note that a new deployment configuration was used on all LOBSTER OBS (except for GEOMAR stations), where custom-made blue tarpaulin sheets secured the buoys towards the frame to minimise rope resonance.

Pool & Type	OBS Type	Seismometer	Datalogger Type	Nr.
DEPAS	LOBSTER	Trillium Compact OBS	K.U.M. 6D6	29
DEPAS N	NAMMU	Trillium Compact OBS	K.U.M. 6D6	3
GEOMAR	LOBSTER	Trillium Compact OBS	K.U.M. 6D6	4
DIAS	NAMMU	Trillium Compact OBS	K.U.M. 6D6	7
ROA-UCM (UP15 & UP21)	LOBSTER	Trillium Compact OBS	Geolon-MCS	2
ROA-UCM (UP23)	LOBSTER	Güralp CMG 40-T	Geolon-MCS	1
IDL (UP07 & UP24)	DUNE	Güralp Certis	Güralp Minimus	2
IDL (UP14* & UP17)	DUNE	Silicon Audio Accelerometer	K.U.M. 6D6	2

* UP14 was not recovered.

Table 2 Summary table of types of OBS, seismometers, and recorders provided for the UPFLOW experiment by the different instrument pools. Note that all instruments were equipped with HTI-04-PCA/ULF hydrophones.

3.1 State-of-Health

In addition to seismometer and hydrophone data, the OBSs also recorded State-of-Health (SOH) data (e.g., recorder temperature, battery voltage, humidity, mass positions, levelling adjustments, magnetic field) that provide essential information about the status of the OBS, allowing a diagnosis of poor or unusable waveform data.

We document SOH for all UPFLOW stations for which auxiliary files are available in the supplementary material. One typical example showing normal instrument behaviour is presented for UP06 in the supplementary material (Fig. S2).

The top panel displays the battery voltage throughout the deployment. As expected, it shows an effectively constant voltage within the 0.05 V quantisation. The second panel shows temperature recordings obtained from both the recorder and seismometer. While the absolute temperature values may differ between the two devices, the SOH figures show that, as expected for normal instrument behaviour, the temperature variations follow the same trend throughout the year, with no substantial variations.

Disparities in temperature recordings between stations could be due to local ocean currents/water masses, local hydrothermal activity, and/or be related to internal processes (Fig. S2-S6, 2nd panel; recorder blue curves; seismometer orange curves). Finally, the third and fourth panels show the mass position (voltage) and static sensor acceleration, respectively, which are, again, quite stable for UP06 overall. The term "static sensor acceleration" refers to the signal that results from the combined response of the seismic mass and the electronic feedback system.

These data can help to determine if the instruments experienced instability or encountered technical issues, as we discuss below in Section 3.2. For instance, if the mass voltage changes or the static sensor acceleration changes during the recording period, it may indicate slight tilting of the instrument, e.g. in OBS12 (Fig. S3) and in UP19 (Fig. S4). While this may or may not directly affect data quality, it can provide insight when data exhibit anomalies potentially originating from current-induced noise.

3.2 Instrument losses and failures

The one OBS lost in the UPFLOW experiment — UP14 — was a DUNE prototype, which did not send any response signals during the recovery procedure and could not be seen at the sea surface despite an extensive ~4 h search in the deployment area.

For other stations, some instrument issues and failures were encountered. Earlier-than-expected battery drainage affected 10 stations (UP07, UP24, X25, OBS12, OBS17, OBS19, UP15, UP19, UP26, UP28; see Fig. S7-S12 for a summary of station uptimes and Fig. S3, S5 and S6 for examples of battery drainage). Power issues with IDL stations were caused by a firmware bug that led to an early shutdown and excessive non-linear clock drift, rendering the data unusable. The GEOMAR battery packs likely did not have sufficient capacity for the planned duration of the recording in a potentially noisy environment. For UP15, battery drainage was accelerated due to frequent levelling checks performed every half hour on the seismometer, due to user-defined settings before deployments. Yet, during the recording period of UP15 and of the GEOMAR stations, the recorded data do not show any substantial issues. The SOH data (e.g. in Figs. S4-S6) were instrumental in understanding issues with station UP19 (Fig. S4). Analysis of the mass voltage and seismometer temperature revealed significant variations (indicated by the orange curve in the second panel), whereas the temperature of the datalogger remained relatively constant (indicated by the blue curve). Discussions with the DEPAS pool leads, based on experience from past experiments, suggested that the OBS might have been moving or tilting on the seabed, requiring excessive power and depleting the batteries faster. In practice, this led to an unexpected interruption of the recording due to a low battery. At the end of the deployment, the recording restarted, following some battery recovery. All these issues led to the data of UP19 not having sufficient quality for further analyses.

On the other hand, the SOH data for stations UP26 and UP28 indicated a normal performance of the seismometers (Figs. S5 and S6), which suggests insufficient capacity of their battery packs at the experiment's outset.

The data from UP10's seismometer were completely unusable due to a corroded connector pin, likely caused by mishandling during deployment, exposing it to seawater and leading to the severe corrosion observed upon recovery. The faulty pin compromised data transmission and partially affected the hydrophone channel. UP23 also did not record any usable seismometer data, indicating a possible malfunction or obstruction of the levelling system. Additionally, no SOH was available for this instrument to check for possible causes of instrument problems. The failure to download these SOH data came from a lack of memory.

All the issues described above result in unusable seismometer data from five stations (UP07, UP10, UP19, UP23, UP24). Yet, these problems are relatively mild given the 50 stations deployed in UPFLOW. Indeed, the overall data completeness (the ratio of theoretically achievable versus recorded data considering all four components) is 91.21 %. This fully accounts for one lost station (0 % recovery) as well as for early recording stops. For instance, if a station only recorded for 6 months instead of for a planned deployment of a full year, this would correspond to 50 % data completeness. All further analyses exclude lost stations or those with faulty data (red stations in Table 1). Excluding those stations, data completeness is 95.5 %.

3.3 Clock drift

Free-fall OBSs are isolated from GPS while on the seafloor, thus, their clocks drift due to temperature variations, clock ageing, and/or thermal hysteresis (e.g., Gardner and Collins 2012). Conventionally, clocks are synchronised with GPS upon deployment and recovery, yielding a "clock skew" measurement. In UPFLOW, it was possible to measure clock skew for all OBSs, except for (i) UP15 due to a human operation error; and (ii) UP30, which had a faulty communication plate in the 6D6 recorder that could not be repaired or replaced during recovery. UP34 had a similar issue but could be rectified onboard, allowing a skew measurement to be taken 15 h after recovery. UP07 and UP24 were severely affected by a firmware issue, which caused extreme clock drifts of >24 h. An incorrect low-power mode caused their internal clocks to start drifting heavily in October 2021.

Table 2 shows that UPFLOW's clock skew ranged between −21.71 s and 7.95 s, with the average absolute skew value being 8.64 s. The two fully functioning OBSs with MCS recorders (UP23 and UP21) achieved much lower skew values (−0.0004 s and 0.52 s, respectively) than their newer 6D6 counterparts. Given that typical errors, for example, in teleseismic body wave travel time measurements are ∼0.3 s for P-waves and up to ∼2.8 s for S waves (e.g., Nolet and van der Lee 2022), UPFLOW's recorded skew values are substantial.

Many OBS studies assume that clock drift is linear during the recording period on the seafloor (e.g., Gardner and Collins 2012). However, deviations from linearity have been reported, including nonlinear skew trends in the RHUM-RUM experiment (Hable et al., 2018). More recently, Cabieces et al. (2024) showed similar nonlinear clock drift behaviour for the UPFLOW experiment. They used continuous recordings of seismic ambient noise and the relative shift of daily Empirical Green's Functions to estimate clock drift curves for 40 UPFLOW OBSs. They found that 95 % of the clock drift observations had a substantial non-linear component, with maximum deviations to linearity up to 2 s. The estimated drift curves had an average uncertainty of ∼0.11 s, indicating the suitability of the drift corrections for future seismological studies, such as seismic tomography and earthquake source analyses.

4 Data formatting and processing

During the UPFLOW recovery expedition in August-September 2022, all data were converted into miniSEED format. Moreover, we built instrument response files in StationXML format following standard procedures (Ahern et al., 2012). Subsequently, we resampled the data to various sampling rates useful for a variety of applications and, thus, obtained several time series data channels (e.g., Long Period LH with 1 samples-per-second (sps) and Broadband BH with 20 sps). We then deconvolved the instrument response following standard procedures using *ObsPy* (Krischer et al., 2015, see details in Section S2 in the supplementary material, notably an illustrative example in Fig. S1). Two essential processing operations were performed: (i) estimating the stations' horizontal component orientations; and (ii) tilt and compliance removal. The next two subsections explain these operations.

4.1 Horizontal component orientations

We employed two classical methods to estimate the horizontal orientation of the OBSs, utilising both body- and surface-waves. The first method relies on the polarisation of long-period teleseismic P-waves (8-30 s), which are expected to predominantly appear on the radial (R) and vertical (Z) components (Niu and Li, 2011; Braunmiller et al., 2020). The second method utilises the elliptical particle motion of Rayleigh waves in the Z-R plane (Stachnik et al., 2012). The P-wave polarisation in the Z-1-2 system is determined through an eigenvalue analysis of the covariance matrix. The associated error bars represent formal 95 % confidence intervals. For the P-wave polarisation, they represent the expected error of the mean based on the empirical variance of measurements for individual events. In turn, the Rayleigh wave orientation is obtained via a grid search approach with 1° increments, which maximises the correlation between the Z component and the Hilbert transform of the R component. Error bars are derived from a combination of bootstrap analysis and averaging of errors obtained from two frequency bands (see supplementary material for details; see Fig. 3 and Table S4).

A total of 149 earthquakes (Fig. S13, Table S1-S3) reported in the GCMT catalogue (Ekström et al., 2012) were initially analysed, and orientation measurements were obtained using 10 to 20 events per station (see Table S4). Due to strict quality control (see Section S6.3 and Figs. S14-S19 in the supplementary materials for details about the quality control measures used) only 27 events contribute to the final orientation estimates. In this analysis, 219 individual P-arrival orientation measurements (including outliers), derived from 24 earthquakes, are employed to estimate sensor orientations for 8 stations with good quality and 28 with poor quality. Estimates for the remaining 11 stations were invalid (see Section S6.1 in the supplementary materials for details about how invalid, poor, and good data quality are defined). Additionally, 399 individual Rayleigh wave orientation measurements, based on 16 earthquakes, were utilised to determine sensor orientations for 37 stations with good quality and 6 with poor quality; only 4 stations had invalid estimates.

Fig. 3 and Table S4 show that for some stations only a few measurements can be extracted from long-period P-wave arrivals, while the Rayleigh wave method can successfully be applied to most stations. In cases where both methods provide robust estimates, we observe a good agreement within the estimated uncertainties (shown as black circles in Fig. 3). Even when one method is considered less reliable due to a small number of contributing events, the results of both methods generally agree within a few degrees. If both P and Rayleigh wave estimates are classified as reliable, the final estimate is defined as the error-weighted mean of the two. Otherwise, the estimate from the other method is used.

For some stations (e.g., UP21, UP28, UP31, UP39, UP46), estimates are uncertain due to the lack of results from one method or reliance on very few observations. Nonetheless, these estimates, though imprecise, are used for setting the metadata entries for station orientation. Some stations (UP40, UP41, UP42) exhibit phase shifts between the vertical and radial components for the P wave arrivals (see Fig. S16). Their physical proximity to each other, south and west of Madeira, suggests a structural reason for this, likely the presence of un- or partially consolidated sediments with a few hundred metres of thickness. In such a setting, the sediment-basement P-to-S conversion will be much stronger on the radial component than the direct P-wave and delayed by 1 s to 2 s, resulting in the observed phase shift. Despite P-wave measurements failing quality checks, estimates based on reliable Rayleigh wave measurements are considered reasonable for these stations. Finally, a tendency towards orientations between approximately 120° and 210° is observed, which is unlikely to arise from chance. However, any explanation for this clustering would be highly speculative and is therefore not further discussed here.

4.2 Seafloor tilt and compliance corrections

Seafloor compliance describes how the seafloor deforms under pressure from waves in the overlying ocean (e.g., low-frequency infragravity waves). We measure compliance as the spectral ratio between pressure and vertical displacement measurements. Compliance noise is possibly the predominant contributor to noise in vertical component OBS data recordings (Crawford and Webb, 2000). Although compliance noise also affects horizontal component data, it is difficult to separate from the effects of other noise sources such as seafloor currents (Webb and Crawford, 1999; Doran and Laske, 2016).

The primary approach for correcting vertical component OBS data for compliance effects entails measuring frequency-dependent pressure changes with a hydrophone or Differential Pressure Gauge (DPG). Based on the spectral coherence in recordings of ambient seismic noise (ideally free from the signal of interest), the transfer function between pressure and vertical component waveforms is calculated. The correction is then performed by applying this transfer function to the recorded pressure data to predict the compliance effect on the vertical component, which is then subtracted to obtain the corrected trace. This procedure was first outlined by Webb and Crawford (1999) and, in this study, we implemented it into the framework of the open-source ISP software (Cabieces et al., 2022).

Another noise source is tilt noise, which will always affect the horizontal components but also arises on the vertical component for OBS stations that are not perfectly levelled. In most cases, the tilt direction (measured on a compass — as opposed to the tilt angle, measured from the vertical axis) is unknown and might vary with time (Bell et al., 2015; Janiszewski et al., 2023), making it hard to carry out the correction deterministically.

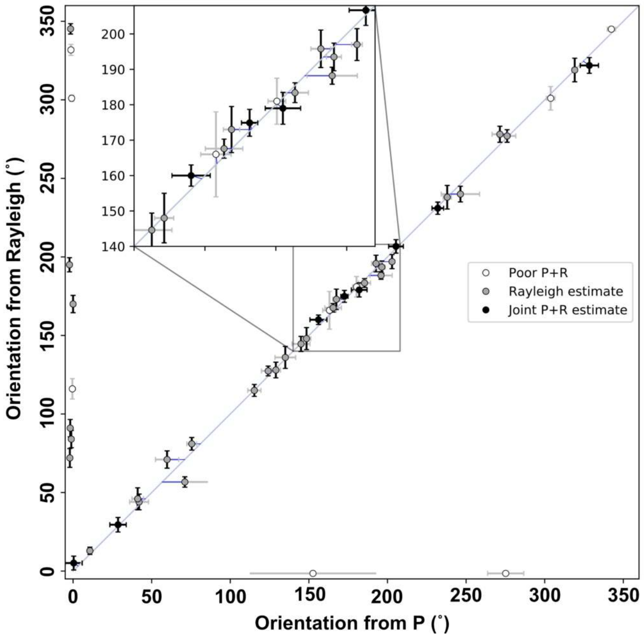

Figure 3 Comparison of estimated orientations of the '1' component (clockwise from North) from polarisation analysis of long-period P-waves (P; T∼8 s to 30 s) and analysis of Rayleigh wave (R; T∼8 s to 20 s) particle motion. Error bars are drawn in black if the estimate and error estimate are considered robust and in grey when the estimate is classed as unreliable. Circles are black if both methods returned reliable results, grey if one of the estimates was deemed unreliable, and white if both methods were classed as unreliable or returned no result at all. Thin blue lines connect to the points on the main diagonal which represent our best final estimate of station orientation. For nine stations, only a Rayleigh wave method estimate could be obtained (UP17, UP21, UP31, UP37, UP39, UP40, UP41, UP42, UP46), and for one station, only a P-wave one (UP28; excluding "invalid-invalid" cases); those results are plotted near the respective coordinate axes.

Instead, this effect can be removed analogously to the compliance removal technique by calculating the transfer functions between the two horizontal components and the vertical component (Crawford and Webb, 2000). Following Crawford and Webb (2000), we combine both tilt and compliance corrections using our implementation in ISP and apply them sequentially to all UPFLOW stations for which there were no major instrument issues or failures (section 3.2) using time windows of 15 min. This choice provides a reasonable compromise between time and frequency resolution to remove the low-frequency tilt and compliance noise (f <0.1 Hz).

This combined tilt and compliance analysis requires all four components: three-component seismometer and pressure (hydrophone) data. We first correct for tilt, which is followed by compliance subtraction. We recompute corrected transfer/coherence functions between tilt-corrected vertical and pressure for compliance corrections, following the cascade procedure of Crawford and Webb (2000). Illustrative results are presented in the next section together with other UPFLOW data examples, as well as in the supplementary materials (Figs. S20–S21). Moreover, the UPFLOW data corrected for tilt and compliance are freely distributed in the EIDA (European Integrated Data Archive) platform, as explained in Section 6.

5 Data quality and examples

Prior to the UPFLOW recovery expedition in 2022, we devised a data quality control (QC) protocol, which consisted of computing and plotting for each station: (i) Probabilistic power spectral density (PPSD, Figs. S22 — S26) for all components over the whole deployment to assess the stations' noise levels and spectra (Table S5 in the supplementary materials includes all the details and parameters used for these calculations); (ii) Illustrative seismic waveforms for a pre-defined list of teleseismic, regional, and local earthquakes (Tables S1-S3); and, (iii) Daily spectrogram throughout the whole deployment to detect other signals (e.g., whales, earthquakes not reported in catalogues, instrumental resonances, etc.; see supplementary material, links in Section S1). In this section, we present examples of these data/spectra. We note that, except for Fig. 7 and Fig. 9, the examples shown are not corrected for tilt and compliance.

5.1 Noise levels

Fig. 4 presents the PPSD acceleration plots (McNamara, 2004; Krischer et al., 2015) for station UP05 (for all individual PPSD please refer to Figs. S22 — S26).

The vertical component (Z) noise levels in both high and low-frequency ranges fall within the boundaries of the New High Noise Model (NHNM) and New Low Noise Model (NLNM) of Peterson (1993), which were obtained using land data. The long-period horizontal component data (T>20 s) are substantially noisier than the NHNM. Hydrophone PSDs were converted to acceleration to ensure comparability with seismic data. Most of the corresponding hydrophone PPSD values fall between the NHNM and the NLNM, except for periods longer than 80 s.

To facilitate the comparison across stations and channels, the median PPSDs computed for all the UPFLOW stations except those with issues discussed in Section 3 are presented in Fig. 5.

For most stations, the vertical component median PPSD falls between the NHNM and the NLNM. The horizontal components show noisier PPSDs, especially in the wave period range 10 s to 100 s. While Fig. 4 shows PPSDs from hydrophone acoustic pressure data converted to acceleration, for completeness, Fig. 5 displays median PPSDs for the actual hydrophone acoustic pressure data, which are compared with the CTBTO high and low noise models (Brown et al., 2014). Most of the UPFLOW hydrophone median PPSDs fall within the CTBTO high and low noise models.

The distribution of hydrophone and vertical seismometer component noise for each station in the 2 s to 12 s band is shown in Fig. 6. For the vertical component, the median station noise lies below the NHNM (indicated by the top red horizontal line) for all stations; it ranges from −135 dB to −105 dB (m^2/s^4/Hz) with

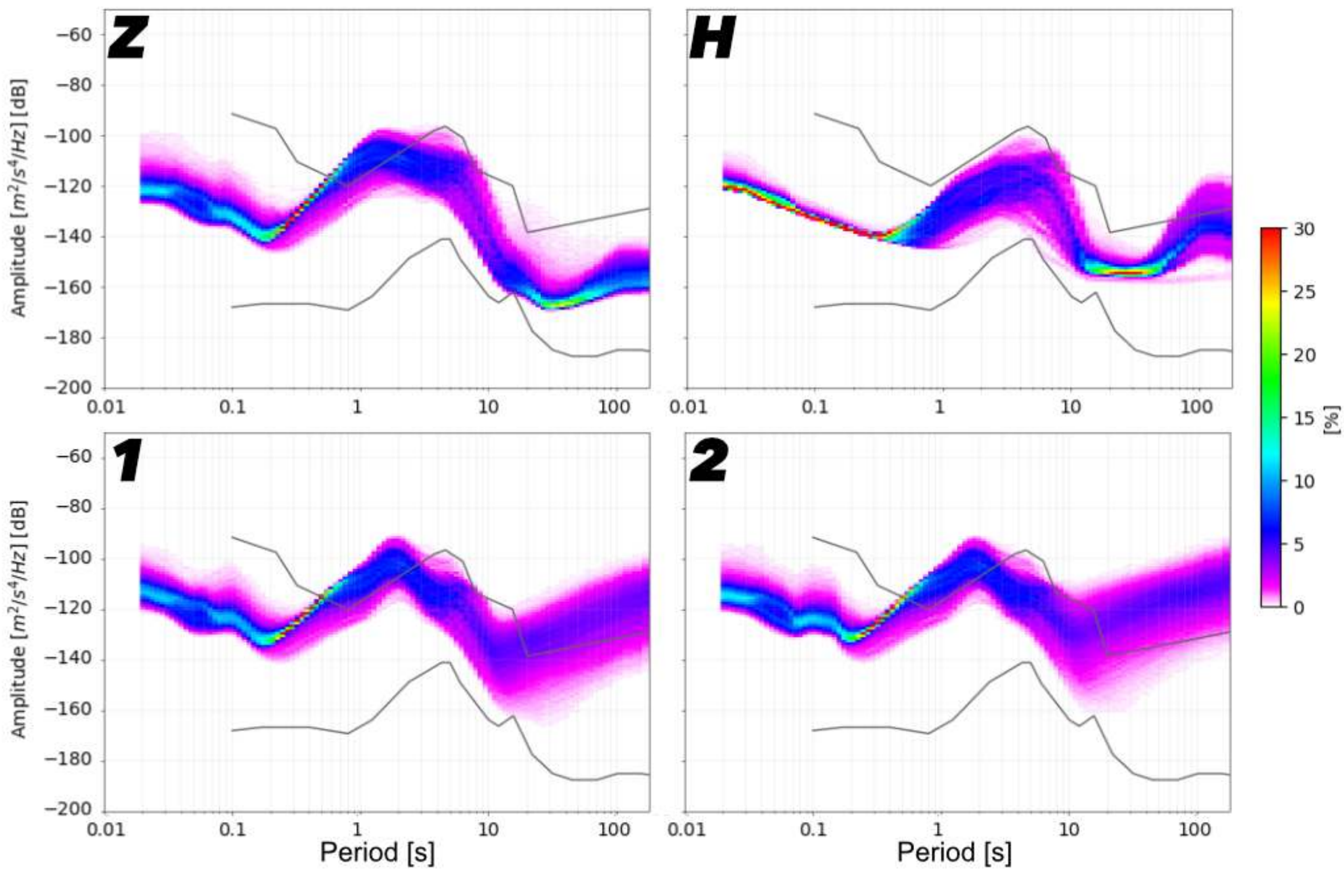

Figure 4 Probabilistic power spectral density (PPSD) for the four channels of station UP05. The PPSD for the vertical component (upper left corner) falls mostly inside the lower and upper land noise model levels (grey lines). On the other hand, the horizontal components (lower panels) are noisier, especially between periods of 10 s and 100 s. The hydrophone noise levels in the upper right corner are usually displayed in the −60 dB to 60 dB range, due to its hydroacoustic nature. We converted the hydrophone PPSD to acceleration-equivalent. The grey lines correspond to the New High Noise Model (NHNM) and New Low Noise Model (NLNM) of Peterson (1993), respectively.

an average value of -120 dB. The median hydrophone noise ranges from −12 dB to 22 dB (Pa^2/Hz) with an average value of +10 dB. The quartiles generally follow the trend of the medians, with some variations, i.e., stations which are typically quiet, tend to be also among the quiet ones on quiet days and noisy days, and vice versa.

As explained in the previous section, we applied tilt and compliance corrections to the vertical component seismometer data. While all the examples of data/spectra presented so far do not include these corrections, Fig. 7 shows the effect of removing tilt and compliance noise from vertical component data for UPFLOW OBS stations (for completeness, we also present the associated inter-channel coherence in Fig. S21). We observe the most substantial noise level reduction for wave periods longer than T$\sim$25 s, and especially for T$>\sim$ 100 s. This is probably due to the strong influence of ocean gravity waves at these periods, particularly infragravity waves arising at internal density contrasts within the water column (Webb et al., 1991; Godin et al., 2013). To further explore the impact of the tilt and compliance corrections on UPFLOW's earthquake waveform data, we calculated the signal-to-noise ratio (SNR) for over 3,700 vertical component recordings of the 149 earthquakes considered in our study (Tables S1 - S3) for waveforms with and without tilt and compliance corrections. The SNR is defined as the root-mean-square (RMS) of the Rayleigh wave window divided by the RMS of the preceding noise window, using the same filtering as in our horizontal orientation analysis (see illustrative waveform examples in Fig. S27). Fig. S27 also presents the distribution of the SNR gain, which is the difference between the SNR of the waveforms with and without tilt and compliance corrections. It shows that in most cases, the SNR gain is small and close to zero. While in some cases the tilt and compliance corrections improve the SNR of the earthquake waveforms, in other cases, it degrades the signal. This is not surprising as our tilt and compliance corrections are more substantial for longer period data than for those used in our horizontal orientation analysis.

5.2 Earthquake recordings

Our list of teleseismic, regional, and local events compiled prior to the expedition included 149 events (see Tables S1 - S3) selected based on their moment magnitude and epicentral distance to the UPFLOW network. We found that 85 % of the earthquakes in our list were cap-

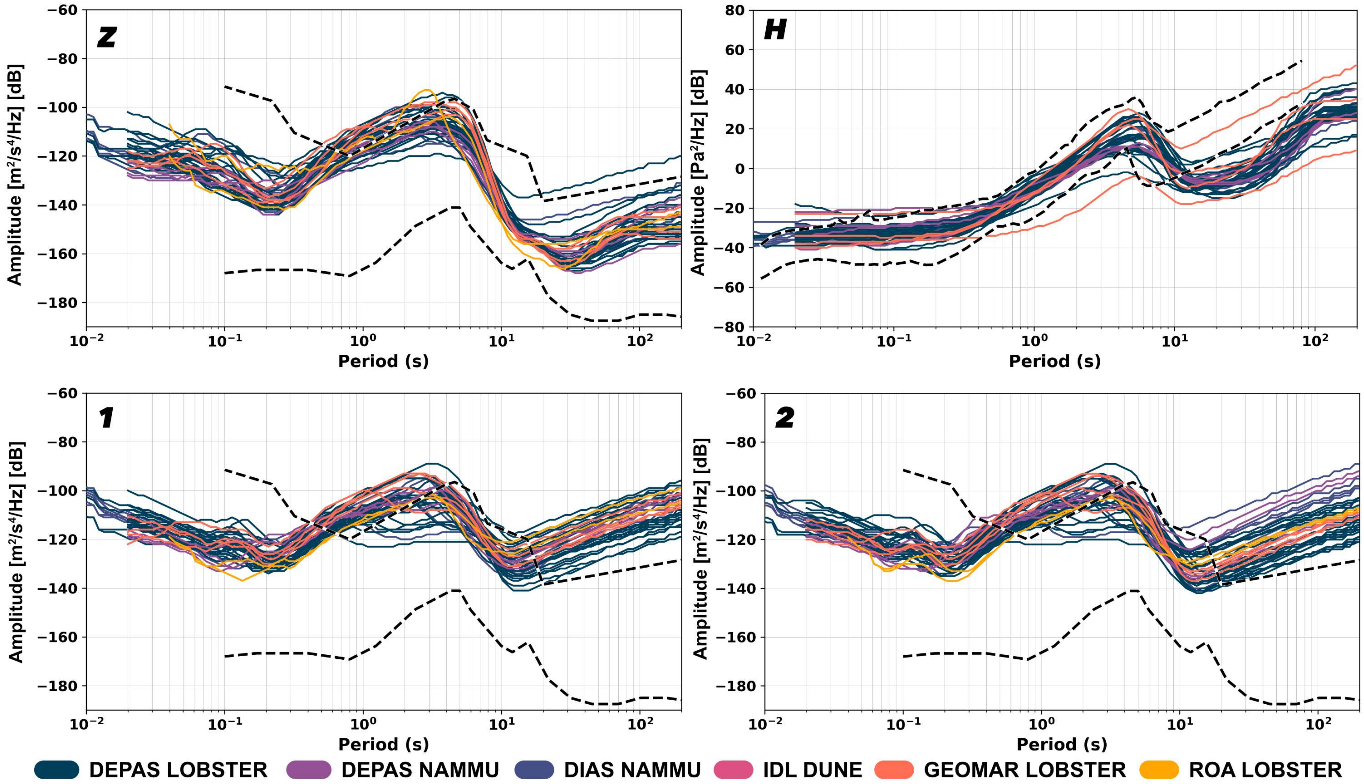

Figure 5 Median PPSDs for all UPFLOW stations with seismometers for which no issues were identified in Section 3 and four channels. For most stations, the vertical component PPSD (upper left corner) falls in between the NHNM and NLNM (dashed grey lines on plots for Z, 1, and 2 components). The horizontal components (lower panels) are noisier, especially between 10 s and 100 s. The hydrophone noise in the upper right corner is displayed between −60 dB and 60 dB (note the difference to the previous figure; here, we do not convert acoustic pressure into acceleration to allow an evaluation of the data directly obtained from the hydrophones); the dashed lines represent the CTBTO hydroacoustic high and low noise models (Brown et al., 2014).

tured by UPFLOW stations, with clear signals in more than 70 % of the stations with seismometers for which no issues were identified in Section 3.

Fig. 8 shows two examples of earthquakes widely recorded by UPFLOW stations (vertical component) for a Mw 7.1 earthquake in the South Sandwich Islands and a ML 1.7 local/regional event in the Gloria Fault region (Fig. 1, red star close to UP07). In both cases, the recordings show waveforms with very clear arrivals of various wave types (P and S waves, Rayleigh waves, and T waves).

In addition to analysing earthquake time series, we also performed spectral analyses (Ferreira et al., 2006) and observed high-quality normal modes (Earth's free oscillations) for the Mw 8.3 2021 South Sandwich Islands earthquake on 12 August 2021 and for the Mw 8.2 Alaska earthquake on 29 July 2021. Fig. 9 shows an illustrative comparison between the original (uncorrected for tilt and compliance) 48-hour normal mode data spectrum for the $\mathrm{M_w}$ 8.3 2021 South Sandwich Islands earthquake with the spectrum obtained for data corrected for compliance and tilt, as explained in Section 4.2. The latter corrections enhance the normal mode observability, with clear normal modes observed down to at least about 1.8 mHz. The majority of UPFLOW vertical component seismometer stations show good quality normal mode observations for both the South Sandwich Islands and the Alaska events, which highlights the high quality of our low-frequency vertical component data. Horizontal component data do not show clear normal modes due to noisier low-frequency data, as presented, e.g., in Fig. 5.

5.3 Non-Earthquake signals

In addition to earthquake recordings, OBS data are rich in many non-earthquake signals potentially valuable for different disciplines such as oceanography and marine biology.

Fig. 10a shows illustrative spectrograms for the vertical channel computed for station UP06 for the whole experimental period. The vertical component spectra show well-known distinct seasonal signals in the microseismic noise band ($T \sim 1$ to 16 s), with enhanced amplitude in winter due to stronger storms in the North Atlantic (Lecocq et al., 2020). Moreover, a clear signal appears during winter around 17 Hz in the spectrogram, which corresponds to blue whale vocalisations and Fig. 10c highlights characteristic fin whale calls (Silva et al., 2013; Pereira et al., 2020, 2021). Marine mammals, such as, e.g., baleen whales with low-frequency vocalisations, produce a variety of sounds for communication, detection (prey/food), and navigation purposes, and these signals can be detected and analysed in OBS seismometer data (Pereira et al., 2020, 2021). Investigat-

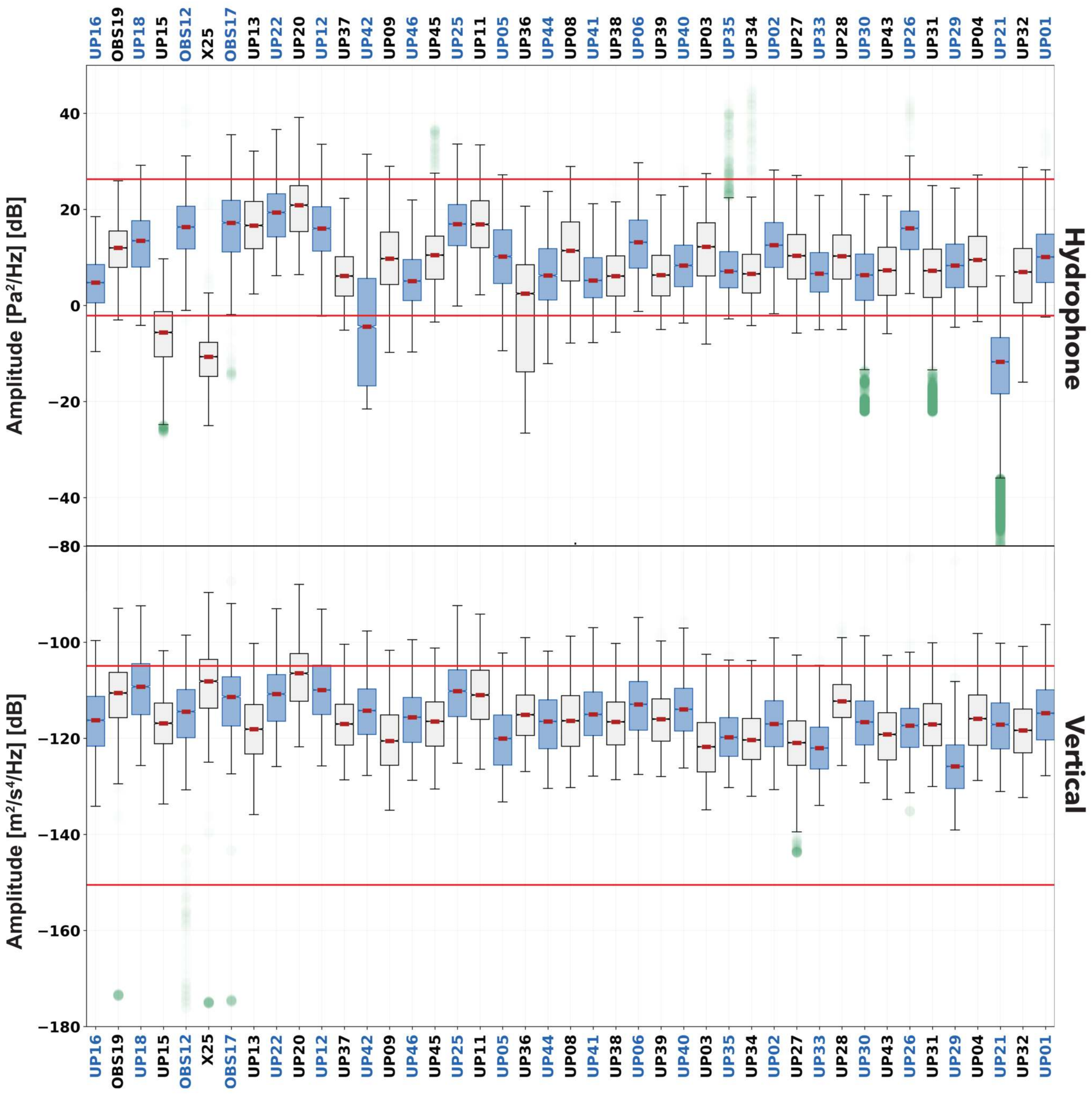

Figure 6 Boxplot of the UPFLOW stations for the hydrophone (top) and vertical component seismometer (bottom) data between 2 s and 12 s, extracted from PPSDs (after Stähler et al. 2016). The minimum and maximum values in the dataset are represented by whiskers, extending vertically up and downwards from the box. Quartiles and median are represented by the closed box and are drawn between the first quartile (Q1) and the third quartile (Q3). The small red rectangles represent the median of the data. Green scatter are outliers, which lie significantly above or below the rest of the data. The horizontal red lines in the top correspond to the CTBTO hydroacoustic high and low noise models (Brown et al., 2014), while in the bottom the NHNM and NLNM land noise models are shown for this particular frequency range (Peterson, 1993).

ing these signals can contribute to our understanding of marine mammals' behaviour, migration patterns, and their interactions with the marine environment.

As explained previously in Section 2, the LOBSTER and NAMMU OBSs have flags, radio antennae, buoys, etc. attached to their frames. All these elements resonate at well-known frequencies (6 Hz, 8 Hz and 10 Hz for the antenna, flag, and head buoy, respectively Corela et al. 2023) when subject to the effects of ocean bottom currents. Fig. 11a shows an illustrative example of such resonances. Data from the GEOMAR OBS19 station, which had a freely floating head buoy, show clear multiple horizontal band signals associated with the buoy in the 1-15 Hz frequency range. These signals are very similar to the signature of the head buoy observed in the RHUM-RUM experiment (Stähler et al., 2016, 2018). On the other hand, such signals are not observed for stations with fixed buoys, leading to reduced noise levels in

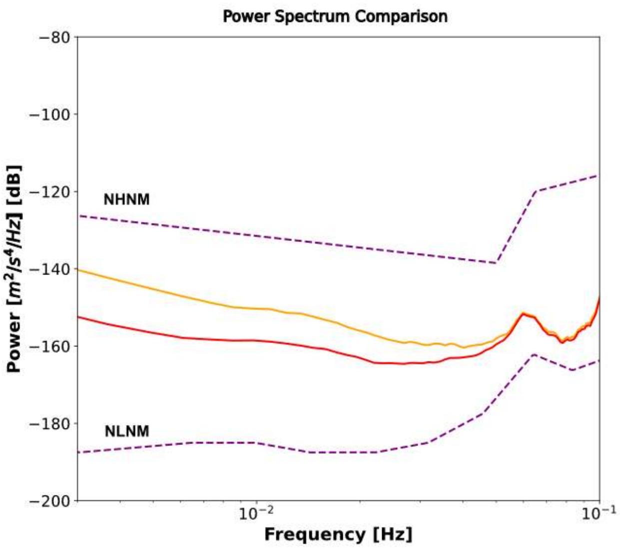

Figure 7 Comparison of average PSDs between raw data (orange) and tilt- and compliance-corrected data (red) for the vertical component. Upper and lower purple lines correspond to the NHNM and NHLM (Peterson, 1993). Fig. S20 shows comparisons of individual power spectra median lines before and after tilt and compliance corrections, and inter-channel coherence is presented in Fig. S21.

the ∼1 Hz to ∼15 Hz frequency range compared to stations with free buoys (Fig. 11b). This shows that wrapping the head buoy reduces strumming and noise.

6 Data archiving and distribution

Professional open data archiving and maintenance are vital to ensure the integrity, safety, utility, and legacy of OBS data, yet they are still not a standard practice. Such practices greatly facilitate the distribution of data among team members during the data embargo period and, subsequently, to the wider community. Moreover, the assignment of Digital Object Identifiers (DOIs) to the data is not only key to ensuring their traceability, but also for promoting proper acknowledgement in scholarly work. FAIR (Findable, Accessible, Interoperable and Reusable) principles are increasingly being adopted in data sharing (Wilkinson et al., 2016), which involve a "Give-and-take" philosophy to ensure fairness, emphasising principles of accessibility and usability.

EIDA (European Integrated Data Archive), an initiative within ORFEUS (Strollo et al., 2021), plays a pivotal role in securely archiving seismic waveform data and metadata from various research infrastructures. EIDA/ORFEUS offer excellent personalised support for data archiving, handles DOI assignments, and strongly promotes the adoption of open and FAIR data policies, which makes them the ideal repository for UPFLOW data.

Given the complexities of handling and preprocessing OBS data (e.g., clock drift corrections), an OBS data working group has proposed modifications to StationXML and miniSEED formats (Clinton et al., 2018). This proposal outlines OBS-specific standards, best practices, and post-processing tools to enhance data clarity and ease of use. While preparing UPFLOW data for the repository in the GFZ EIDA node (Ferreira, 2024), we have followed these proposed principles. We filled the various recommended fields in the StationXML files using the same values as presented in Table 1. For example, a "Localisation method" field is recommended to indicate how the OBS position was determined. Additionally, we provide the on-deck GPS deployment coordinates. In the "Measurement method" field, we describe how parameters such as, e.g., azimuth and dip were determined (see Section 4.1). The non-linear clock drift corrections, which were obtained by Cabieces et al. (2024) (Section 3.3), are applied to the data by correcting daily files for clock drift. Finally, key details are summarised in the "Comment" field of the StationXML file or abstract in the Digital Object Identifier (DOI), offering a quick reference point for users seeking essential information about the dataset. If leap seconds occur, they are corrected and explicitly flagged to maintain temporal accuracy in archived data, but none occurred during the UPFLOW experiment.

Archived UPFLOW data include BH (Broadband, sampling rate 50 Hz), HH (High Broadband, sampling rate 100 Hz) or CH (sampling rate 250 Hz) channels, depending on the original sampling rate during the deployment. An additional LH (Long-Period, sampling rate 1 Hz) channel is also distributed. Since LH data are typically used in long-period seismic studies, which may greatly benefit from tilt and compliance corrections, we apply these corrections to the vertical component LH data as explained in Section 4. We do not distribute uncorrected vertical component LH data for simplicity since such data can be easily obtained by decimating, e.g., BH data.

7 Discussion

7.1 Instrument performance

In this study, we examined auxiliary data that are usually not shown or discussed in the scientific literature, notably the instrument's State of Health (SOH) information (e.g., levelling adjustments, magnetometer data, changes due to the instrument's reorientation, battery voltage, temperature, mass position and acceleration), which inform about the seismometers' operational state throughout the experiment.

SOH data have been crucial to pin down, for example, the causes for premature termination of the recordings, such as insufficient capacity of the battery packs at the experiment's outset. Moreover, we found that one station (UP19) possibly landed on unstable ground in the seabed, leading to regular movement and tilting throughout the recording period. This information is key to giving us strong confidence in the data acquired in the case of insufficient battery capacity, which did not show particularly anomalous SOH data throughout the experiment (e.g., for UP26 and UP28), while a more cautious approach is needed when using data from UP19. Hence, our study clearly shows that the availability of SOH data along with their systematic quantitative anal-

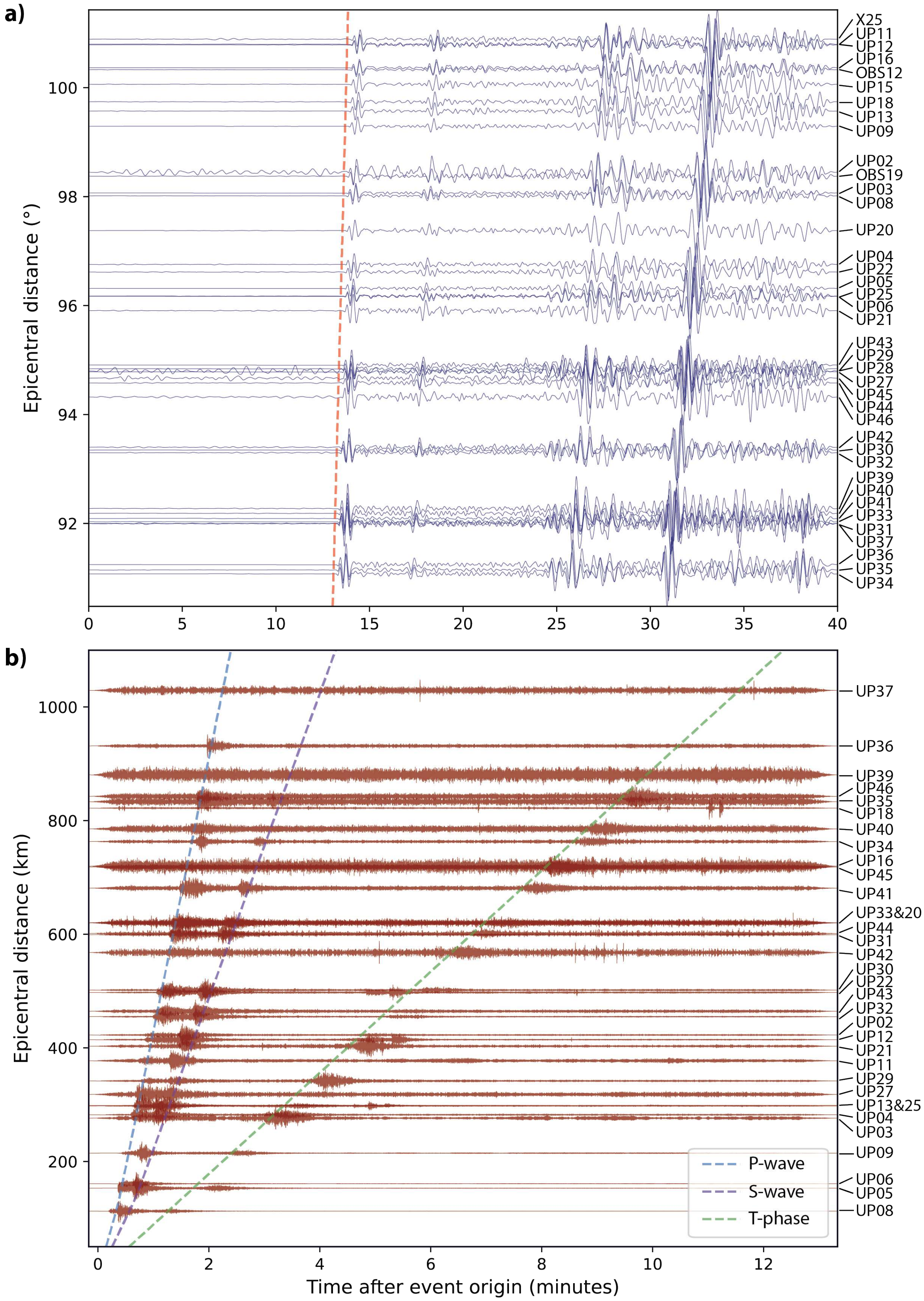

Figure 8 Record sections of vertical component seismometer recordings for earthquakes recorded by the UPFLOW network. a) A teleseismic $\mathrm{M_w} \sim$7.1 earthquake in the South Sandwich Islands at 2021-08-22T21:33:13. The orange dashed line denotes the theoretical arrival times of the first-arriving P-wave calculated for the Earth model iasp91 (Kennett and Engdahl, 1991). Traces are bandpass filtered between 20 s and 50 s period. b) A local $\mathrm{M_l} \sim$1.7 event on the western segment of the Gloria Fault Zone on 2022-06-29T02:31:43 (epicentre shown by the red star in Fig. 1), as reported in the IPMA earthquake catalogue. Traces are bandpass filtered between 5 Hz and 15 Hz.

ysis is very useful for a comprehensive assessment of the quality of OBS data. Given the huge costs typically involved in the acquisition of these datasets, SOH data analysis allows a more complete understanding of these

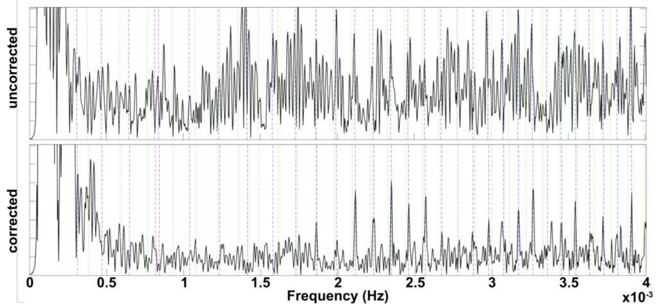

Figure 9 Comparison between the original 48 hr normal mode data spectrum for the M_w 8.3 2021 South Sandwich Islands earthquake (top) and the spectrum obtained for data corrected for compliance and tilt (bottom) for station UP01 (vertical component). The vertical dashed lines correspond to theoretical normal mode eigenfrequencies for the PREM model (Dziewonski and Anderson, 1981), with blue lines corresponding to spheroidal modes, green lines being for toroidal modes, and the red line representing the $_0S_0$ mode. See Section 5.2 in the main text for more information.

precious data.

A major issue with the UPFLOW data was the large clock skew values observed, being on average 8.64 s in absolute value over the experiment duration. This required a meticulous, time-consuming ambient noise clock drift analysis (Cabieces et al., 2024), which identified substantial non-linear clock drift, with deviations from non-linearity going up to ∼1 s to ∼2 s. Such substantial non-linearity is significant for many common seismological applications (e.g., seismic tomography, seismicity studies, etc). Recent open software tools for clock drift analyses (e.g., Naranjo et al., 2024; Cabieces et al., 2024) will help accelerate future OBS clock drift analyses. Moreover, future work on new instrument development (e.g., using atomic clocks with optimised power consumption) may greatly reduce OBS clock drift issues (Lodewyk et al., 2014).

7.2 OBS data noise levels

The landscape of studies publishing OBS data quality and issues is sparse compared to the actual number of experiments (e.g., Sumy et al., 2015; Stähler et al., 2016; Barcheck et al., 2020; Eilon et al., 2021; Parisi et al., 2024), making it challenging to benchmark our findings against others. For older experiments, some information can be found in cruise reports (open or closed access). Stähler et al. (2016) have set a precedent by providing a detailed account of OBS data quality and instrument performance. However, some limitations persist, notably the paucity of opportunities for comparing data from different experiments. The work of Janiszewski et al. (2023) is commendable in this regard, offering a comprehensive comparison of data from various OBS experiments. They performed a systematic analysis of OBS noise as a function of seismometer type and deployment water depth, mostly using OBS data collected in the Pacific Ocean. Fig. 12 compares the noise levels of UPFLOW's OBS stations from the vertical components with the results of Janiszewski et al. (2023). The long period (>5 s) OBS noise levels reported by Janiszewski et al. (2023) span a wide range within the high (NHNM) and low noise model (NLNM) of Peterson (1993), with in particular shallow stations at <3000 m depth regularly exceeding the NHNM. In contrast, the data noise levels observed in UPFLOW tend to fall close to the lower end of the spread of prior measurements. Notably, there seems to be little dependence of noise levels on water depth. Lower noise levels compared to previous experiments are likely due to a combination of enhanced sensors, larger water depths, and local environmental conditions (e.g., deep ocean currents).

As expected, the horizontal component data are noisier than the vertical component data (Figs. 4, S22-S26), particularly for long-period data (T>20 s), where they exceed the high noise model (NHNM). Yet, compared with previous experiments, such as the DOCTAR experiment near the Gloria Fault (Fig. S28), we observe an overall noise reduction in periods from 1 s to 10 s. DOCTAR performs better at higher frequencies on the horizontal components, but in both the DOCTAR and UPFLOW experiments, the horizontal components are noisy. Hence, we consider horizontal data recorded by UPFLOW to be of reasonable quality compared to other OBS data. Moreover, it is worth highlighting that, as explained in Section 4.1, robust horizontal component rotation angles were determined during UPFLOW's recovery expedition, without requiring subsequent re-analyses, additional earthquakes used, etc. A total of 149 earthquakes from a list compiled before the expedition was used as a starting point, with about 10 to 20 events being used for orientation angle estimates per station (see Table S4). These numbers of events are similar to those utilised in other OBS studies with similar deployment duration (Laske, 1995; Stachnik et al., 2012; Scholz et al., 2017), regardless of their different geographical locations and varying numbers of available earthquakes (e.g., due to regional seismicity patterns).

The data noise levels across different instrument types used in the UPFLOW experiment (see Fig. 2, 6 and 12) are overall similar. This is akin to the findings of Stähler et al. (2016) for the RHUM-RUM experiment and shows that noise sources (e.g., microseismic noise, oceanic currents, etc.) influence all stations broadly in a similar way. It should just be noted that, in specific frequency bands, differences in noise levels do occur between different instruments or deployment practices, such as with the GEOMAR LOBSTER OBSs displaying higher noise levels than other UPFLOW LOBSTER's from around 5 Hz to 20 Hz due to their free head buoy (Section 5.3).

As explained in Section 5.3, wrapping and fixing the head buoy in the DEPAS and ROA-UCM LOBSTER's with custom-made tarps substantially reduced well-documented head buoy-induced reverberations, leading to noise levels similar to those observed for NAMMU instruments (which also have the head buoy tucked aside the OBS frame during data acquisition; see Fig. 2). Hence, this study strongly supports tucking away the head buoy in existing LOBSTER instruments where it is loose by default.

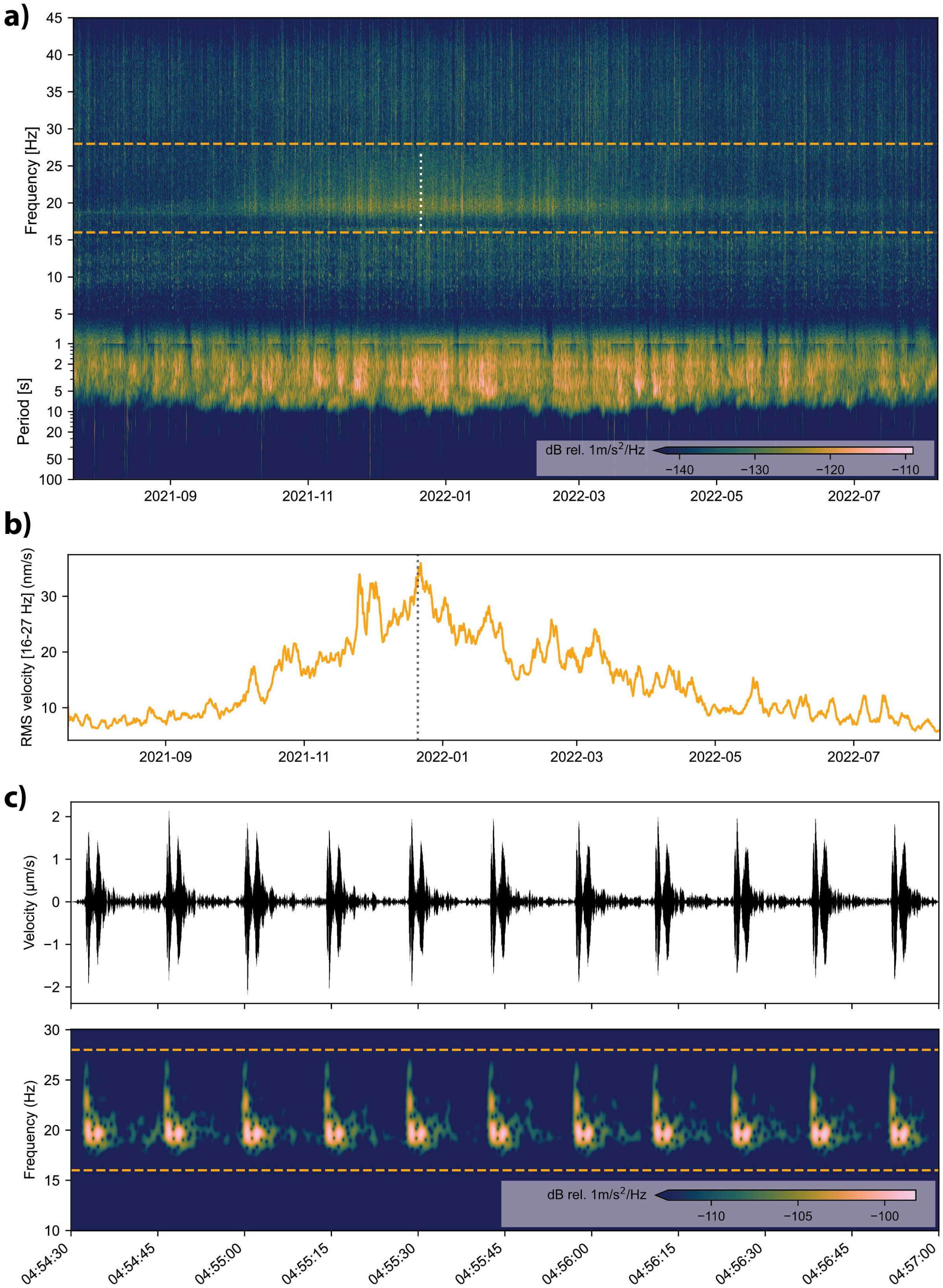

Figure 10 Microseismic noise and whale-call recordings. a) Spectrogram for the vertical component of station UP06 for its entire recording time. At periods of 1 s to 10 s, there is an increase in the strength and bandwidth of microseismic noise during winter due to storms. Moreover, a clear signal at 16 Hz to 28 Hz (demarcated by the orange dashed lines) emerges during the winter months. b) Corresponding root-mean-square ground velocity in 16 Hz to 28 Hz band (Lecocq et al., 2020), smoothed with 3-day rolling mean. In (a) and (b), the vertical dotted line corresponds to the date of the data segment shown in (c). Two-and-a-half minute long data segment from UP06.HHZ on 2021-12-21 showing 11 characteristic fin whale calls as waveforms in the time domain (top panel; bandpass filtered at 16 Hz to 28 Hz) and as a spectrogram (bottom panel).

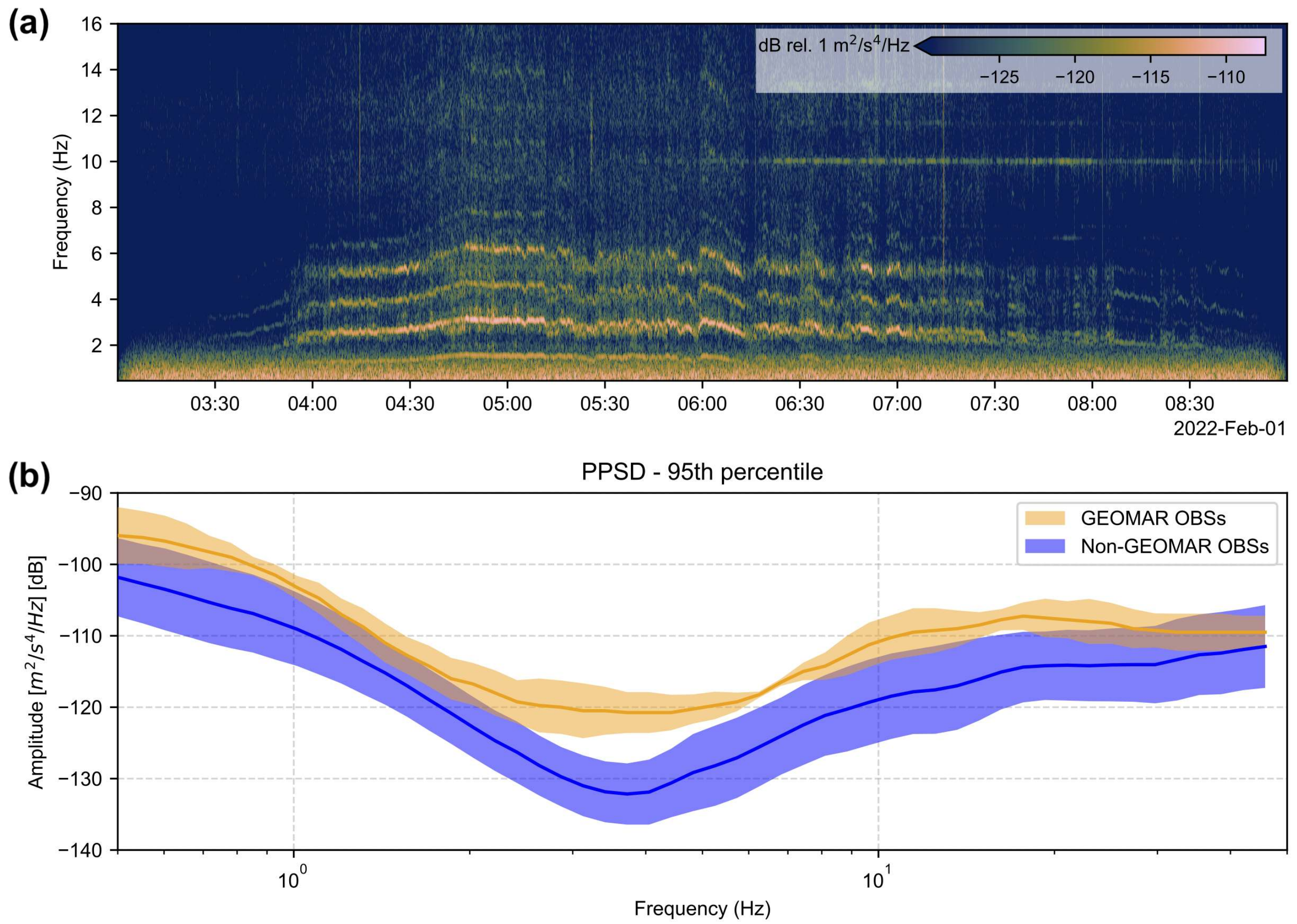

Figure 11 Buoy strumming effect. (a) Vertical-component spectrogram for a 6-hour period from the OBS19, a GEOMAR LOBSTER with a freely floating head buoy affected by ocean currents, leading to the interpreted gliding, strumming signals. These signals are characterised by a gradual rise around 04:00, and subsequent decline around 07:30, and are seen most strongly at, but not limited to, frequencies of 1 Hz to 8 Hz. (b) Comparison between the 95th percentile of high-frequency PPSDs for OBSs with freely-floating heads (GEOMAR type) and those with fixed buoys. The solid lines represent the mean PPSDs for all OBSs, with the shaded areas indicating the standard deviation. The buoy strumming effect leads to an elevated median PPSD curve for all GEOMAR OBSs (yellow line) between ~3 Hz and ~8 Hz compared to the other LOBSTER OBSs (blue line).

Additionally, the flag and the radio antenna exhibit distinct tremor signals at around 1 Hz and 6 Hz, respectively (Corela et al., 2023). Examples of these signals in the UPFLOW data can be found in Fig. 11; unlike for the head buoy, there is currently no easy way to reduce these signals during data acquisition. Hence, it is crucial to consider all these reverberations, which vary depending on the OBS design, when analysing and interpreting OBS data.

Although hydrophone data are commonly available in most OBS experiments, their underutilisation for analysis is a prevailing issue. A comparison of our hydrophone noise levels with Stähler et al. (2016) reveals remarkable similarity in the period range (T ~2 s to 12 s), between 0 dB and 20 dB, in the boxplot analysis. Both studies show consistent frequency-dependent noise variations between −40 dB and 40 dB despite different environmental settings. Yet, comparing our hydrophone observations with those from Janiszewski et al. (2023) poses additional complexities due to the diverse dataset encompassing both differential pressure gauges (DPGs) and absolute pressure gauges (APGs).

Differences in hydrophone data might be due to their response information or pressure gauges displaying calibration issues, where it might be necessary to adjust the amplitudes to reach a good agreement between different datasets (Janiszewski et al., 2023).

7.3 Earthquake and non-earthquake observations

We presented illustrative examples of UPFLOW's high-quality recordings of teleseismic and local earthquakes, including good-quality observations of Earth's free oscillations (normal modes). While some previous OBS studies reported observations of low-frequency normal modes (Bécel et al., 2011; Laske et al., 2007; Laske, 2021), which are some of the most demanding observations in broadband seismology (Laske, 2021), they were mostly obtained using very broadband instruments (e.g., using Trillium 240 broadband sensors). To the best of

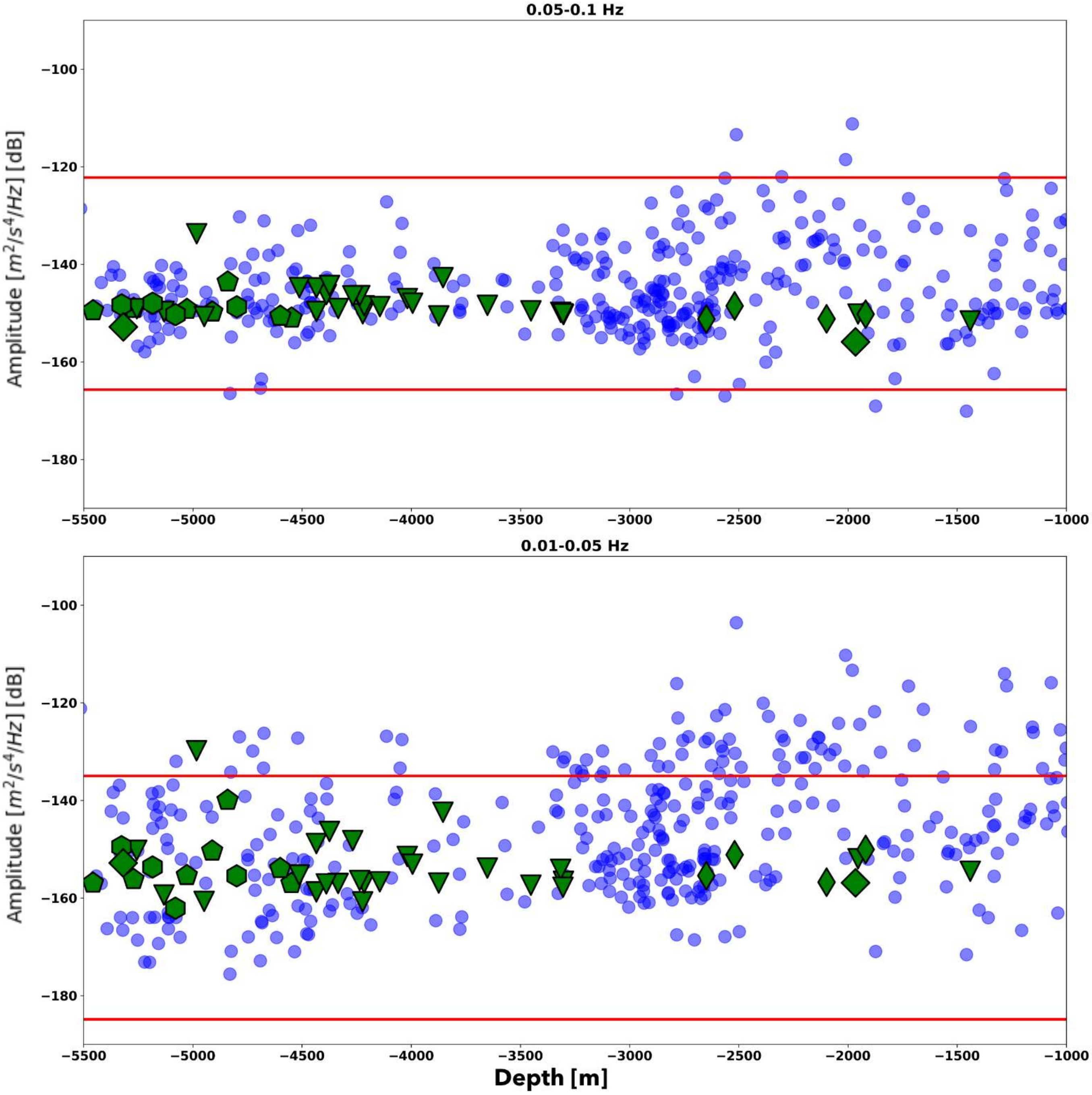

Figure 12 Comparison of vertical component seismometer noise levels (y-axis) versus water depth (x-axis) for UPFLOW stations (green symbols) and for a compilation of recordings from the Pacific Ocean (light blue dots) by Janiszewski et al. (2023). The downward triangle represents DEPAS LOBSTER, the hexagon DEPAS NAMMU, the pentagon represents DIAS NAMMU, the thin diamond shows GEOMAR, the diamond represents ROA-UCM, and the square represents IDL stations. Note that UPFLOW data tends to aggregate at the lower noise levels reported by Janiszewski et al. (2023), especially for the shallower water depths. Noise levels are shown in the 0.05 Hz to 0.1 Hz (top) and the 0.01 Hz to 0.05 Hz (bottom) frequency ranges. Horizontal red lines represent the median high (NHNM) and low noise model (NLNM) (Peterson, 1993) for that frequency range.

our knowledge, our observations are the first clear report of OBS low-frequency normal modes observed using Trillium Compact instruments (with a corner period of 120 s). This highlights the complementarity of these sensors to very broadband instruments for low-frequency OBS studies. Moreover, we found that it was straightforward to apply tilt and compliance corrections (Crawford and Webb, 2000; Bell et al., 2015; Cabieces et al., 2022) to all the UPFLOW data. This reduced the noise levels of the low-frequency recordings (f<0.04 Hz; Fig. 7), notably enhancing the quality of the normal mode observations. Future studies will investigate in detail the information encapsulated in these corrections, notably possible constraints on near-surface seismic structures contained in our compliance estimates. In addition, other techniques have been developed to reduce OBS data noise, notably for normal mode observations (e.g., Harmon et al., 2022), which will be interesting to explore in future work.

While performing our systematic spectrogram and time series analysis of UPFLOW data during the recovery cruise, we found surface waves from some teleseismic events that were not originally anticipated, including magnitudes down to M_w ~5.2 at distances as large as 137°. We are currently working on the detection and compilation of all seismic events recorded by UPFLOW, which exceeds the scope of this study. More generally, given the low vertical noise levels documented in this study and the high-quality recordings of earthquakes, including normal mode observations, it is clear that UPFLOW data are highly suitable for future tomography, seismicity, moment tensor, and various other studies.

Many non-earthquake signals were also recorded, such as whale vocalisations (e.g., fin and blue whales), which were clearly observed both in hydrophone and seismometer data. The vocalisation recordings are more prevalent during the winter recording period, suggesting a relationship with whale migration patterns. Given the large geographical extent and duration of the UPFLOW experiment, Saoulis et al. (2026) developed a novel machine learning model based on 2-D semantic segmentation to efficiently identify current-induced instrument resonances as well as blue whale calls across the array. The UPFLOW data along with this machine learning model will be beneficial for future studies of whale populations and behaviour, and their relationship with environmental noise (e.g., ship noise). Reverberations from OBS components (e.g., from the flag, beacon, flasher, etc.) are also ubiquitous in the UPFLOW data. While it is currently difficult to change the OBS design to reduce these reverberations, they offer an interesting opportunity to study the characteristics of deep ocean currents, which are the main source of excitation of these reverberations.

8 Conclusions

UPFLOW successfully deployed 50 OBSs and recovered 49 OBSs from the seafloor in the Azores-Madeira-Canaries islands region between June 2021 and August 2022. Data completeness of ~91% was achieved, with only three out of 49 instruments failing and two others exhibiting serious firmware issues. This paper focused on a quality assessment of the UPFLOW data and showed a reduced noise level compared to previous studies of similar scope, notably for long-period vertical component data. Moreover, horizontal component data showed reasonable quality, with noise levels similar to or lower than previous OBS experiments, enabling the estimation of their orientation angles using both body and surface waves from teleseismic events. Furthermore, clear Earth normal modes with frequencies as low as ~1.8 mHz for two M_w 8 events were observed, with their visibility being enhanced by tilt and compliance corrections.

Data quality was improved compared to previous comparable experiments by modified deployment procedures (i.e., by fixing the head buoy in the majority of the LOBSTER instruments) and by the use of new sensors (upgrade from Güralp CMG-OBS40T to Nanometrics Trillium Compact sensors).

Overall, the data quality achieved will enable future seismic imaging studies of the UPFLOW region to better understand the nature and origin of mantle upwelling in the region and, more generally, at the global scale.

Additional signals recorded by the UPFLOW array throughout the whole experiment include vocalisations from baleen whales (e.g., fin and blue whales) and OBS parts reverberations, which will be useful for investigating deep ocean currents. Given the good quality, richness, and quantity of seismic and acoustic pressure recordings obtained for the first time in such a large area of the Atlantic Ocean, UPFLOW data offer an unprecedented opportunity to address many open questions, not only in geology and geodynamics, but also in other disciplines such as oceanography and marine biology.

Acknowledgements

The UPFLOW project is funded by the ERC Horizon Fund (grant agreement 101001601). Additional support is provided by IPMA. DEPAS LOBSTER's and NAMMUs were provided by "Deutscher Geräte-Pool für Amphibische Seismologie" at Alfred-Wegener-Institut (Bremerhaven, Germany). We thank Henning Kirk for the exceptional preparation of DEPAS instruments, which has been instrumental to our work. We also thank the captain and crew of the research vessel Mario Ruivo for their excellent support during deployment and recovery. Special thanks go to the Dublin Institute for Advanced Studies (DIAS, Ireland) for providing NAMMU instruments, ROA-UCM (Cádiz and Madrid, Spain) and GEOMAR (Kiel, Germany) for their generous provision of LOBSTER OBSs, and Instituto Dom Luiz (IDL, Lisbon, Portugal) for their contribution of the DUNE instrument to the UPFLOW project.

C.Corela, J.L. Duarte and A.Loureiro were funded by the DUNE project (grant number:PTDC/EAM-OCE/28389/2017) and by the Portuguese Fundação para a Ciência e a Tecnologia (FCT) I.P. / MCTES through national funds (PIDDAC) – UIDB/50019/2020, UIDP/50019/2020 and LA/P/0068/2020.

Figures were predominantly produced with the ObsPy software (Krischer et al., 2015). We thank the EIDA node operated by the GEOFON data centre of the GFZ (German Research Centre for Geosciences, Potsdam) for hosting the UPFLOW data. We would like to extend our thanks to Susanne Hemmleb and Angelo Strollo for helping to upload the UPFLOW data and set up the metadata. EIDA is a part of ORFEUS.

Additionally, we acknowledge the steadfast support received from IPMA before, during, and after the UPFLOW cruise.

Data and code availability

The UPFLOW data are archived in the GFZ EIDA node (network code 8J 2021-2023, Ferreira, 2024) and will be embargoed until the end of April 2028. All software used in this manuscript is freely available.

CSV files of daily data coverage and quality were prepared, and a full description can be found in the Supplementary Section S11, along with illustrative figures

S29 - S30. The files offer a machine-readable summary of daily data coverage and quality for each station and component, helping users quickly assess the dataset and identify any potential anomalies prior to download or further processing. Further, we provide an extended version of Table S4 in CSV format.

Competing interests

The authors declare no competing interests.

References

Ahern, T., Casey, R., Barnes, D., Benson, R., and Knight, T. SEED Reference Manual – standard for the exchange of earthquake data. http://www.fdsn.org/pdf/SEEDManual_V2.4.pdf, 2012.

Barcheck, G., Abers, G. A., Adams, A. N., Bécel, A., Collins, J., Gaherty, J. B., Haeussler, P. J., Li, Z., Moore, G., Onyango, E., Roland, E., Sampson, D. E., Schwartz, S. Y., Sheehan, A. F., Shillington, D. J., Shore, P. J., Webb, S., Wiens, D. A., and Worthington, L. L. The Alaska Amphibious Community Seismic Experiment. *Seismological Research Letters*, 91(6):3054–3063, 08 2020. doi: 10.1785/0220200189.

Beier, C., Haase, K. M., and Abouchami, W. Geochemical and geochronological constraints on the evolution of the Azores Plateau. *Origin, Evolution, Environmental Impact of Oceanic LIPs*, 511, 2015.

Bell, S. W., Forsyth, D. W., and Ruan, Y. Removing Noise from the Vertical Component Records of Ocean-Bottom Seismometers: Results from Year One of the Cascadia Initiative. *Bulletin of the Seismological Society of America*, 105(1):300–313, Feb. 2015. doi: 10.1785/0120140054.

Braunmiller, J., Nabelek, J., and Ghods, A. Sensor Orientation of Iranian Broadband Seismic Stations from P-Wave Particle Motion. *Seismological Research Letters*, 91(3):1660–1671, May 2020. doi: 10.1785/0220200019.

Brown, D., Ceranna, L., Prior, M., Mialle, P., and Le Bras, R. J. The IDC Seismic, Hydroacoustic and Infrasound Global Low and High Noise Models. *Pure and Applied Geophysics*, 171(3-5): 361–375, Mar. 2014. doi: 10.1007/s00024-012-0573-6.

Bécel, A., Laigle, M., Diaz, J., Montagner, J.-P., and Hirn, A. Earth's free oscillations recorded by free-fall OBS ocean-bottom seismometers at the Lesser Antilles subduction zone: NORMAL MODES RECORDED BY OBS. *Geophysical Research Letters*, 38 (24):n/a–n/a, Dec. 2011. doi: 10.1029/2011GL049533.

Cabieces, R., Olivar-Castaño, A., Junqueira, T. C., and Relinque, J. Integrated Seismic Program (ISP): A new Python GUI-based software for earthquake seismology and seismic signal processing. *Seismological Research Letters*, 93:1895–1908, 2022. doi: 10.1785/0220210205.

Cabieces, R., Harris, K., Ferreira, A. M. G., Tsekhmistrenko, M., Hicks, S. P., Krüger, F., Geissler, W. H., Hannemann, K., and Schmidt-Aursch, M. C. Clock Drift Corrections for Large Aperture Ocean Bottom Seismometer Arrays: Application to the UPFLOW Array in the Mid-Atlantic Ocean. *Geophysical Journal International*, 239(3):1709–1728, 2024. doi: 10.1093/gji/ggae354.

Cannat, M., Briais, A., Deplus, C., Escartin, J., Georgen, J., Lin, J., Mercouriev, S., Meyzen, C., Muller, M., Pouliquen, G., et al. Mid-Atlantic Ridge–Azores hotspot interactions: along-axis migration of a hotspot-derived event of enhanced magmatism 10 to 4 Ma ago. *Earth and Planetary Science Letters*, 173(3):257–269, 1999.

Civiero, C., Custódio, S., Neres, M., Schlaphorst, D., Mata, J., and Silveira, G. The role of the seismically slow Central-East Atlantic Anomaly in the genesis of the Canary and Madeira volcanic provinces. *Geophysical Research Letters*, pages 1–15, 2021. doi: 10.1029/2021gl092874.

Clinton, J., Crawford, W., Evangelidis, C., Kaestli, P., Gueguen, P., Pedersen, H., Quinteros, J., Saurel, J.-M., Sleeman, R., and Strollo, A. Report on metadata challenges and proposed solutions. www.sera-eu.org/export/sites/sera/home/.galleries/Deliverables/SERA_D4.2_Metadata-challenges-and-proposed-solutions.pdf, 2018. Work package WP4 "Expanding access to the European seismic monitoring infrastructure", Submission date 31.10.2018.

Corela, C., Loureiro, A., Duarte, J. L., Matias, L., Rebelo, T., and Bartolomeu, T. The effect of deep ocean currents on ocean-bottom seismometers records. *Natural Hazards and Earth System Sciences*, 23:1433–1451, 2023. doi: 10.5194/nhess-23-1433-2023.

Crawford, W. C. and Webb, S. C. Identifying and Removing Tilt Noise from Low-Frequency (<0.1 Hz) Seafloor Vertical Seismic Data. *Bulletin of the Seismological Society of America*, 90: 952–963, 2000. doi: 10.1785/0119990121.

Doran, A. K. and Laske, G. Infragravity waves and horizontal seafloor compliance. *Journal of Geophysical Research: Solid Earth*, 121(1):260–278, 2016. doi: 10.1002/2015JB012511.

Dziewonski, A. M. and Anderson, D. L. Preliminary reference Earth model. *Physics of the Earth and Planetary Interiors*, 25(4): 297–356, 1981. doi: 10.1016/0031-9201(81)90046-7.

Eilon, Z. C., Gaherty, J. B., Zhang, L., Russell, J., McPeak, S., Phillips, J., Forsyth, D. W., and Ekström, G. The Pacific OBS Research into Convecting Asthenosphere (ORCA) Experimente. *Seismological Research Letters*, 93:477–493, 2021. doi: 10.1785/0220210173.

Ekström, G., Nettles, M., and Dziewoński, A. The global CMT project 2004–2010: Centroid-moment tensors for 13,017 earthquakes. *Physics of the Earth and Planetary Interiors*, 200:1–9, 2012. doi: 10.1016/j.pepi.2012.04.002.

Essing, D., Schlindwein, V., Schmidt-Aursch, M. C., Hadziioannou, C., and Stähler, S. C. Characteristics of Current-Induced Harmonic Tremor Signals in Ocean-Bottom Seismometer Records. *Seismological Research Letters*, 92(5):3100–3112, 04 2021. doi: 10.1785/0220200397.

FDSN Web Services. FDSN Web Services, n.d. https://www.fdsn.org/webservices/. Accessed: 2025-01-05.

Ferreira, A. M. G. Upward mantle flow from novel seismic observations (UPFLOW)., 2024. doi: 10.14470/3W055238.

Ferreira, A. M. G., d'Oreye, N. F., Woodhouse, J. H., and Zürn, W. Comparison of fluid tiltmeter data with long-period seismograms: Surface waves and Earth's free oscillations. *Journal of Geophysical Research: Solid Earth*, 111(B11), 2006. doi: 10.1029/2006JB004311.

Ferreira, A. M. G., Miranda, M., Baranbooei, S., Diaz, R. C., Carapuço, M., Corela, C., Duarte, J. L., Gentry, A., Ferreira, H., Geissler, W. H., Harris, K., Hicks, S., Hosseini, K., Ke, K.-Y., Krüger, F., Lange, D., Loureiro, A., Makus, P., Marignier, A., Neres, M., Ramos, L., Rein, T., Saoulis, A. A., Schlaphorst, D., Tilmann, F., and Tsekhmistrenko, M. Charting the Mantle Beneath the Waves: A Multinational Seafloor Seismology Experiment Across the Mid-Atlantic. *Astronomy & Geophysics*, 2026.

Gardner, A. T. and Collins, J. A. Advancements in high-performance timing for long-term underwater experiments: A comparison of chip scale atomic clocks to traditional microprocessor-compensated crystal oscillators. In *2012 Oceans*, pages 1–8. IEEE, 2012. doi: 10.1109/OCEANS.2012.6404847.

Genske, F. S., Beier, C., Stracke, A., Turner, S. P., Pearson, N. J., Hauff, F., Schaefer, B. F., and Haase, K. M. Comparing the nature of the western and eastern Azores mantle. *Geochimica et*

Cosmochimica Acta, 172:76–92, 2016.

Gente, P., Dyment, J., Maia, M., and Goslin, J. Interaction between the Mid-Atlantic Ridge and the Azores hot spot during the last 85 Myr: Emplacement and rifting of the hot spot-derived plateaus. *Geochemistry, Geophysics, Geosystems*, 4(10), 2003.

Godin, O. A., Zabotin, N. A., Sheehan, A. F., Yang, Z., and Collins, J. A. Power spectra of infragravity waves in a deep ocean. *Geophysical Research Letters*, 40(10):2159–2165, 2013.

Hable, S., Sigloch, K., Barruol, G., Stähler, S. C., and Hadziioannou, C. Clock errors in land and ocean bottom seismograms: high-accuracy estimates from multiple-component noise cross-correlations. *Geophysical Journal International*, 214:2014–2034, 2018. doi: 10.1093/gji/ggy236.

Harmon, N., Laske, G., Crawford, W., and Rychert, C. Tilt Corrections for Normal Mode Observations on Ocean Bottom Seismic Data, an Example from the PI-LAB Experiment. *Seismica*, 1(1), 2022. doi: 10.26443/seismica.v1i1.196.

Hosseini, K. and Sigloch, K. ObspyDMT: a Python toolbox for retrieving and processing large seismological data sets. *Solid Earth*, 8(5):1047–1070, 2017. doi: 10.5194/se-8-1047-2017.

Janiszewski, H. A., Eilon, Z., Russell, J. B., Brunsvik, B., Gaherty, J. B., Mosher, S. G., Hawley, W. B., and Coats, S. Broad-band ocean bottom seismometer noise properties. *Geophysical Journal International*, 233:297–315, 2023. doi: 10.1093/gji/ggac450.

Kennett, B. and Engdahl, E. Traveltimes for global earthquake location and phase identification. *Geophysical Journal International*, 105(2):429–465, 1991. doi: 10.1111/j.1365-246X.1991.tb06724.x.

Krischer, L., Megies, T., Barsch, R., Beyreuther, M., Lecocq, T., Caudron, C., and Wassermann, J. ObsPy: a bridge for seismology into the scientific Python ecosystem. *Computational Science and Discovery*, 8(1):014003, May 2015. doi: 10.1088/1749-4699/8/1/014003.

Laske, G. Global observation of off-great-circle propagation of Long-Period surface waves. *Geophysical Journal International*, 123(1):245–259, Oct. 1995. doi: 10.1111/j.1365-246X.1995.tb06673.x.

Laske, G. Observations of Earth's Normal Modes on Broadband Ocean Bottom Seismometers. *Frontiers in Earth Science*, 9: 679958, June 2021. doi: 10.3389/feart.2021.679958.

Laske, G., Orcutt, J. A., Collins, J. A., Detrick, R. S., Wolfe, C. J., Solomon, S. C., Bercovici, D. A., and Hauri, E. H. Broadband Ocean Bottom Instruments Record Earth's Free Oscillations during the Hawaiian PLUME Experiment. In *AGU Fall Meeting Abstracts*, volume 2007, pages S23A–1107, Dec. 2007.

Lecocq, T., Hicks, S. P., Van Noten, K., Van Wijk, K., Koelemeijer, P., De Plaen, R. S., Massin, F., Hillers, G., Anthony, R. E., Apoloner, M.-T., et al. Global quieting of high-frequency seismic noise due to COVID-19 pandemic lockdown measures. *Science*, 369(6509): 1338–1343, 2020. doi: 10.1126/science.abd2438.

Lodewyk, J., Sumy, D., Evers, B., and Woodward, B. Cascadia Amphibious Array Ocean Bottom Seismograph Instrument Performance, 2014. Last retrieved April 2024.

Marignier, A., Ferreira, A. M., and Kitching, T. The Probability of Mantle Plumes in Global Tomographic Models. *Geochemistry, Geophysics, Geosystems*, 21, 2020. doi: 10.1029/2020GC009276.

McNamara, D. E. Ambient Noise Levels in the Continental United States. *Bulletin of the Seismological Society of America*, 94(4): 1517–1527, Aug. 2004. doi: 10.1785/012003001.

Montelli, R., Nolet, G., Dahlen, F., Masters, G., Engdahl, E. R., and Hung, S.-H. Finite-frequency tomography reveals a variety of plumes in the mantle. *Science*, 303(5656):338–343, 2004.

Naranjo, D., Parisi, L., Jonsson, S., Jousset, P., Werthmaller, D., and Weemstra, C. Ocean Bottom Seismometer Clock Correction using Ambient Seismic Noise. *Seismica*, 3(1), 2024. doi: 10.26443/seismica.v3i1.367.

Neves, M., Miranda, J., and Luis, J. The role of lithospheric processes on the development of linear volcanic ridges in the Azores. *Tectonophysics*, 608:376–388, Nov. 2013. doi: 10.1016/j.tecto.2013.09.016.

Niu, F. and Li, J. Component azimuths of the CEArray stations estimated from P-wave particle motion. *Earthquake Science*, 24(1): 3–13, Feb 2011. doi: 10.1007/s11589-011-0764-8.

NOAA National Centers for Environmental Information. ETOPO 2022 15 Arc-Second Global Relief Model. https://doi.org/10.25921/fd45-gt74, 2022. NOAA National Centers for Environmental Information.

Nolet, G. and van der Lee, S. Error estimates for seismic body wave delay times in the ISC-EHB Bulletin. *Geophysical Journal International*, 231(3):1739–1749, 2022.

Parisi, L., Augustin, N., Trippanera, D., Kirk, H., Dannowski, A., Matrau, R., Fittipaldi, M., Nobile, A., Zielke, O., Valero Cano, E., Hoogewerf, G., Aspiotis, T., Manzo-Vega, S., Espindola Carmona, A., Barreto, A., Juchem, M., Suhendi, C., Schmidt-Aursch, M., Mai, P. M., and Jónsson, S. The First Network of Ocean Bottom Seismometers in the Red Sea to Investigate the Zabargad Fracture Zone. *Seismica*, 3(1), 2024. doi: 10.26443/seismica.v3i1.729.

Pereira, A., Harris, D., Tyack, P., and Matias, L. Fin whale acoustic presence and song characteristics in seas to the southwest of Portugal. *The Journal of the Acoustical Society of America*, 147 (4):2235–2249, Apr. 2020. doi: 10.1121/10.0001066.

Pereira, A., Romagosa, M., Corela, C., Silva, M. A., and Matias, L. Source Levels of 20 Hz Fin Whale Notes Measured as Sound Pressure and Particle Velocity from Ocean-Bottom Seismometers in the North Atlantic. *Journal of Marine Science and Engineering*, 9 (6):646, June 2021. doi: 10.3390/jmse9060646.

Peterson, J. R. Observations and Modeling of Seismic Background Noise. Technical Report 93-322, U.S. Geological Survey, 1993. doi: 10.3133/ofr93322.

Ryan, W. B., Carbotte, S. M., Coplan, J. O., O'Hara, S., Melkonian, A., Arko, R., Weissel, R. A., Ferrini, V., Goodwillie, A., Nitsche, F., et al. Global multi-resolution topography synthesis. *Geochemistry, Geophysics, Geosystems*, 10(3), 2009.

Saoulis, A., Loureiro, A., Tsekhmistrenko, M., and Ferreira, A. M. G. Semantic segmentation for feature detection in ocean bottom seismometer data. *Seismica*, 5(1), Feb. 2026. doi: 10.26443/seismica.v5i1.1821.

Schlömer, A., Geissler, W. H., Jokat, W., and Jegen, M. Hunting for the Tristan mantle plume – An upper mantle tomography around the volcanic island of Tristan da Cunha. *Earth and Planetary Science Letters*, 462:122–131, 2017. doi: 10.1016/j.epsl.2016.12.028.

Schmidt-Aursch, M. C. and Haberland, C. DEPAS (Deutscher Geräte-Pool für amphibische Seismologie): German Instrument Pool for Amphibian Seismology. *Journal of large-scale research facilities JLSRF*, 3:A122, Nov. 2017. doi: 10.17815/jlsrf-3-165.

Scholz, J.-R., Barruol, G., Fontaine, F. R., Sigloch, K., Crawford, W. C., and Deen, M. Orienting ocean-bottom seismometers from *P* -wave and Rayleigh wave polarizations. *Geophysical Journal International*, 208(3):1277–1289, Mar. 2017. doi: 10.1093/gji/ggw426.

Silva, M. A., Prieto, R., Jonsen, I., Baumgartner, M. F., and Santos, R. S. North Atlantic Blue and Fin Whales Suspend Their Spring Migration to Forage in Middle Latitudes: Building up Energy Reserves for the Journey? *PLoS ONE*, 8(10):e76507, Oct. 2013. doi: 10.1371/journal.pone.0076507.

Silveira, G., Stutzmann, E., Davaille, A., Montagner, J.-P., Mendes-Victor, L., and Sebai, A. Azores hotspot signature in the upper mantle. *Journal of Volcanology and Geothermal Research*, 156: 23–34, 8 2006. doi: 10.1016/j.jvolgeores.2006.03.022.

Stachnik, J. C., Sheehan, A. F., Zietlow, D. W., Yang, Z., Collins, J., and Ferris, A. Determination of New Zealand Ocean Bottom Seismometer Orientation via Rayleigh-Wave Polarization. *Seismological Research Letters*, 83(4):704–713, July 2012. doi: 10.1785/0220110128.

Strollo, A., Cambaz, D., Clinton, J., Danecek, P., Evangelidis, C. P., Marmureanu, A., Ottemöller, L., Pedersen, H., Sleeman, R., Stammler, K., Armbruster, D., Bienkowski, J., Boukouras, K., Evans, P. L., Fares, M., Neagoe, C., Heimers, S., Heinloo, A., Hoffmann, M., Kaestli, P., Lauciani, V., Michalek, J., Odon Muhire, E., Ozer, M., Palangeanu, L., Pardo, C., Quinteros, J., Quintiliani, M., Antonio Jara-Salvador, J., Schaeffer, J., Schloemer, A., and Triantafyllis, N. EIDA: The European Integrated Data Archive and Service Infrastructure within ORFEUS. *Seismological Research Letters*, 92(3):1788–1795, Mar. 2021. doi: 10.1785/0220200413.

Stähler, S. C., Sigloch, K., Hosseini, K., Crawford, W. C., Barruol, G., Schmidt-Aursch, M. C., Tsekhmistrenko, M., Scholz, J. R., Mazzullo, A., and Deen, M. Performance report of the RHUM-RUM ocean bottom seismometer network around La Réunion, western Indian Ocean. *Advances in Geosciences*, 41:43–63, 2016. doi: 10.5194/adgeo-41-43-2016.

Stähler, S. C., Schmidt-Aursch, M. C., Hein, G., and Mars, R. A self-noise model for the German DEPAS OBS pool. *Seismological Research Letters*, 89:1838–1845, 2018. doi: 10.1785/0220180056.

Sumy, D. F., Lodewyk, J. A., Woodward, R. L., and Evers, B. Ocean-bottom seismograph performance during the Cascadia Initiative. *Seismological Research Letters*, 86(86):1238–1246, 2015. doi: 10.1785/0220150110.

The Portuguese Institute for Sea and Atmosphere, I. P. . . https://www.ipma.pt/en/oipma/quem/ipma/, 2023.

Webb, S. C. and Crawford, W. C. Long period seafloor seismology and deformation under ocean waves. *Bul. Seism. Soc. Am.*, 89 (6):1535–1542, 1999. doi: 10.1785/BSSA0890061535.

Webb, S. C., Zhang, X., and Crawford, W. Infragravity waves in the deep ocean. *Journal of Geophysical Research: Oceans*, 96(C2): 2723–2736, 1991.

Wilkinson, M., Dumontier, M., and Aalbersberg, I. e. a. The FAIR Guiding Principles for scientific data management and stewardship. *Sci Data*, 3(160018), 2016. doi: 10.1038/sdata.2016.18.

Wolfe, C. J., Solomon, S. C., Laske, G., Collins, J. A., Detrick, R. S., Orcutt, J. A., Bercovici, D., and Hauri, E. H. Mantle Shear-Wave Velocity Structure Beneath the Hawaiian Hot Spot. *Science*, 326 (5958):1388–1390, Dec. 2009. doi: 10.1126/science.1180165.

Yang, T., Shen, Y., van der Lee, S., Solomon, S. C., and Hung, S.-H. Upper mantle structure beneath the Azores hotspot from finite-frequency seismic tomography. *Earth and Planetary Science Letters*, 250(1-2):11–26, 2006.